Is there a semi-molten layer at the base of the lunar mantle?

Michaela Walterová[1], Marie Běhounková[2], Michael Efroimsky[3]

[1]Institute of Planetary Research, German Aerospace Center (DLR), Berlin, Germany
[2]Department of Geophysics, Faculty of Mathematics and Physics, Charles University, Prague, Czech Republic
[3]US Naval Observatory, Washington DC, USA

Key Points:

- A lunar mantle governed by the Andrade model fits selenodetic constraints only with a very weak frequency dependence of tidal dissipation
- We seek the parameters of the Sundberg-Cooper model that would explain the anomalous frequency dependence of tidal Q measured by LLR
- Both a dissipative basal layer and elastically-accommodated grain-boundary sliding in the deep mantle result in the same tidal response

Corresponding author: Michaela Walterová, kanovami@gmail.com

Abstract

Parameterised by the Love number k_2 and the tidal quality factor Q, and inferred from lunar laser ranging (LLR), tidal dissipation in the Moon follows an unexpected frequency dependence often interpreted as evidence for a highly dissipative, melt-bearing layer encompassing the core-mantle boundary. Within this, more or less standard interpretation, the basal layer's viscosity is required to be of order 10^{15} to 10^{16} Pa s and its outer radius is predicted to extend to the zone of deep moonquakes. While the reconciliation of those predictions with the mechanical properties of rocks might be challenging, alternative lunar interior models without the basal layer are said to be unable to fit the frequency dependence of tidal Q.

The purpose of our paper is to illustrate under what conditions the frequency-dependence of lunar tidal Q can be interpreted without the need for deep-seated partial melt. Devising a simplified lunar model, in which the mantle is described by the Sundberg-Cooper rheology, we predict the relaxation strength and characteristic timescale of elastically-accommodated grain boundary sliding in the mantle that would give rise to the desired frequency dependence. Along with developing this alternative model, we test the traditional model with basal partial melt; and we show that the two models cannot be distinguished from each other by the available selenodetic measurements. Additional insight into the nature of lunar tidal dissipation can be gained either by measurements of higher-degree Love numbers and quality factors or by farside lunar seismology.

Plain Language Summary

As the Moon raises ocean tides on the Earth, the Earth itself gives rise to periodic deformation of the Moon. Precise measurements of lunar shape and motion can reveal those deformations and even relate them to our natural satellite's interior structure. In this work, we discuss two interpretations of those measurements. According to the first one, the lunar interior is hot and there is a thick layer of partial melt or other weak material buried more than 1000 km deep under the lunar surface. According to the second one, there is no such layer, and the measured deformation can be explained by the behaviour of solid rocks at relatively low temperatures. We show that the two possibilities cannot be distinguished from each other by the existing data.

1 Motivation

Fitting of the lunar laser ranging (LLR) data to the quality-factor power scaling law $Q \sim \chi^p$ rendered a small *negative* value of the exponential: $p = -0.19$ (Williams et al., 2001). Further attempts by the JPL team to reprocess the data led to $p = -0.07$. According to Williams and Boggs (2009),

" *Q for rock is expected to have a weak dependence on tidal period, but it is expected to decrease with period rather than increase.* "

The most recent estimates of the tidal contribution to the lunar physical librations (Williams & Boggs, 2015) still predict a mild increase of Q with period: from $Q = 38 \pm 4$ at one month to $Q = 41 \pm 9$ at one year, yielding $p = -0.03 \pm 0.09$.

Efroimsky (2012a, 2012b) suggested that since the frequency-dependence of k_2/Q always has a kink shape, like in Figure 1, the negative slope found by the LLR measurements could be consistent with the peak of the kink residing between the monthly and annual frequencies. This interpretation entails, for a Maxwell or Andrade moon, very low values of the mean viscosity, indicating the presence of partial melt.

Our goal now is to devise an interpretation based on the Sundberg-Cooper model. Within that model, the kink contains not one but two peaks, and we are considering the possibility that the negative slope of our interest is due to the monthly and annual frequencies bracketing either this peak or the local inter-peak minimum. (It is unlikely that both of these frequencies are located on the negative-slope side of the peak, because the slope of that peak is too steep.)

2 Introduction

2.1 Overview of Previous Works

The knowledge of the interior structure of the Moon is essential for understanding its thermal, geochemical, and orbital evolution as well as the coupled evolution of the Earth-Moon system. The proximity of our natural satellite to the Earth has also made it a frequent target of geophysical exploration. A large amount of data was collected by lunar seismic stations, deployed by the Apollo missions, that were functional for several years between 1972 and 1977 (for a review, see, e.g., Garcia et al., 2019; Nunn et al., 2020). Other constraints are being placed by selenodetic measurements or by geochemical and petrological considerations. However, the deepest interior of the Moon still remains somewhat mysterious. Although different models based on the inversion of seismic travel times generally agree on the lunar mantle structure down to $\sim 1200\,\mathrm{km}$, below these depths they start to diverge greatly (Garcia et al., 2019).

After the acquisition of the first data by the lunar seismic network, it was pointed out by Nakamura et al. (1973, 1974) that direct shear-waves from the farside of the Moon are not being detected by some of the near-side seismometers. Moreover, deep moonquakes, a class of tidally-triggered seismic events originating at around 1000 km depth, were almost absent on the farside. This puzzling phenomenon was interpreted by Nakamura et al. (1973) as an indication for a shear-wave shadow zone caused by a highly attenuating region around the core. Later, Nakamura (2005) reported his further efforts to find farside moonquakes among the discovered nests of deep moonquakes. Having had identified about 30 nests likely to be on the farside, his updated analysis still demonstrated that either the region of the Moon's deep interior within about 40 degrees from the antipodes (the centre of the farside) is nearly aseismic or a portion of lunar lower mantle severely attenuates or deflects seismic waves. Lunar seismic data were also reprocessed by Weber et al. (2011) and Garcia et al. (2011). However, while Weber et al. (2011) also found evidence for deep mantle layering and a strongly attenuating zone at the mantle base, Garcia et al. (2011) did not include such a feature in their lunar interior model. The discussion about the seismic evidence for a strongly attenuating zone is thus still ongoing (Garcia et al., 2019).

Several authors argued for the existence of a low-velocity zone (LVZ) at the base of the mantle also on other than seismological grounds. They linked it to partial melting in deep lunar interior, which might be triggered either by tidal dissipation (Harada et al., 2014), or by the presence of incompatible, radiogenic elements buried after an ancient mantle overturn. The idea of an overturn has been suggested by numerical modelling of magma ocean solidification with the emplacement of ilmenite-bearing cumulates above core-mantle boundary. Moreover, it is potentially supported by observations of near-surface gravity anomalies (Zhang et al., 2013).

Evidence for a low-rigidity/low-viscosity zone has also been sought in the lunar libration signal obtained by LLR (e.g., Williams et al., 2001; Williams & Boggs, 2015), and in selenodetic measurements (including orbiter tracking) that are sensitive to the lunar gravity field and tidal deformation (e.g., Konopliv et al., 2013; Lemoine et al., 2013). One of the most surprising findings resulting from fitting the LLR data was the low value and unexpected frequency dependence of the tidal quality factor Q, as mentioned in Section 1 above. The inferred frequency dependence can be explained by a low effective vis-

cosity of the Moon (Efroimsky, 2012a, 2012b), or by the presence of a secondary peak in the dissipation spectrum (e.g., Williams & Boggs, 2015), possibly caused by the putative basal layer (Harada et al., 2014; Matsumoto et al., 2015). Earlier results from LLR indicated that the lunar core-mantle boundary (CMB) might still be out of equilibrium, which would imply long relaxation times and high lower-mantle viscosities, in contradiction to the presence of a partial melt. However, this hypothesis is not supported by more recent evaluations of LLR data (Viswanathan et al., 2019), showing a CMB at hydrostatic equilibrium.

Despite relative consistency of the evidence for and the theoretical expectation of a highly dissipative basal layer, alternative models of a "melt-free" Moon have been proposed (Nimmo et al., 2012; Karato, 2013; Matsuyama et al., 2016). One argument for high values of lower-mantle viscosities comes from the observations of deep moonquakes. Kawamura et al. (2017) reevaluated an ensemble of moonquakes occurring at depths between 750 and 1200 km and found a brittle-ductile transition temperature of approximately 1240 – 1275 K, implying a cold lunar interior with temperatures below solidus of dry peridotite. Moreover, the employment of a realistic, microphysically substantiated models of the tidal response (Nimmo et al., 2012) can explain the low tidal Q and the observed k_2 of the Moon without requiring the existence of a weak basal layer, which is necessitated in some of the other studies by the model settings and the simplified rheological assumptions.

A feature of the selenodetic measurements that is difficult to explain without the existence of a highly dissipative basal layer is the aforementioned frequency dependence of the lunar Q, repeatedly derived from LLR measurements in the series of works by Williams et al. (2001); Williams and Boggs (2009); Williams et al. (2014), and Williams and Boggs (2015). Even an independent implementation of the LLR software by Pavlov et al. (2016) predicts the same value of Q for the monthly period as for the annual period, which is still not consistent with the expected frequency dependence of tidal dissipation in melt-free silicates.

In the absence of other than LLR-based data on the lunar Q, the most plausible explanation for the unexpected frequency dependence might still be an observational uncertainty, rather than an effect contained in a tidal model. Nevertheless, in this work, we shall explore two possible implications of the frequency dependence under the explicit assumption that the fitted values are a result of a natural phenomenon and not of a model's limitations or an observation error.

2.2 A Putative Weak Basal Layer: Pros and Contras

The following paragraphs review the last ten years of discussion about the presence or absence of a low-viscosity basal layer, with the argumentation derived mainly from the lunar tidal response.

We begin by noting that a negative value of the exponent in $Q \sim \chi^p$ is impossible for the *seismic* quality factor of rocks obeying simple rheologies like the Maxwell or Andrade models. This can be easily understood if we express the seismic Q via the real and imaginary parts of the complex compliance (Efroimsky, 2015, eqn 46). By inserting into this expression either the Maxwell model or any other simple model lacking peaks, we obtain a monotonic function $Q(\chi)$. On the other hand, even for simple rheologies the exponential p can assume negative values if we are fitting to the $Q \sim \chi^p$ law not a seismic but a *tidal* quality factor (Efroimsky, 2015, eqn 45). The tidal Q tends to zero at both very low and very high loading frequencies χ, and has a maximum in between. The maximum is called into being by interplay of rheology and self-gravity.

This theoretical frequency dependence of the tidal quality factor motivated Efroimsky (2012a, Section 5.2) to hypothesise that the small negative exponent p reported by Williams et al. (2001) and Williams and Boggs (2009) may result from a proximity of the major

tidal frequencies in the Moon to the frequency delimiting the peak dissipation. Efroimsky (2012a, Section 5.7) also noted that this interpretation would imply a low effective viscosity of the Moon (modeled with a homogeneous body governed by the Maxwell or the combined Maxwell-Andrade rheology), with an estimated value of $\eta = 3 \times 10^{15}$ Pa s. Such a low viscosity would support seismic models containing a layer of partial melt (Nakamura et al., 1974; Weber et al., 2011).

Nimmo et al. (2012) aimed at answering the question whether basal partial melt is indeed required for reproducing the tidal data, and studied the effect of lunar thermal structure on the seismic and tidal Q. They described the rheology of the lunar interior with the extended Burgers model of Jackson et al. (2010), which contains an absorption band corresponding to high-temperature background, as well as an additional low-temperature peak. The peak represents the elastically-accommodated grain boundary sliding, a phenomenon that will be considered also in our work, although within another rheology. Nimmo et al. (2012) further considered a radially heterogeneous elastic structure of the mantle and accounted for the temperature-, pressure-, and grain-size-dependence of the characteristic relaxation times. Using this model, they were able to match the tidal Love numbers k_2 and h_2 and the monthly quality factor, and they also deduced that the lower-mantle viscosity should be as high as 10^{23} Pa s and must be increasing towards the surface. However, the model used did not succeed in fitting the unexpected slope of Q as a function of frequency. Although the authors showed that a model case with grain size of 1 mm (instead of their baseline value of 1 cm) would imply a negative value of the exponential, $p = -0.02$, they dismissed this model as a poor fit to both k_2 and Q. Moreover, they argued that the smaller grain size would not match the tentative observation of unrelaxed CMB (Williams et al., 2012).

An original explanation of the high tidal dissipation in the Moon was provided by Karato (2013), who linked the measurements of electrical conductivity and Q to the water content in the lunar mantle. That the water content might not be as low as had been presumed in earlier models was illustrated by geochemical studies of lunar samples, and Karato (2013) combined this observation with his own results to propose a new theory of lunar formation. Using the observational constraints on Q and electrical conductivity, he further concluded that the temperature at a 800 km depth of the lunar mantle is $\sim$ 1200–1500 K for a water content between 10^{-3} and 10^{-2} wt.%. Karato (2013) was sceptical to the idea of partial melting at the base of the lunar mantle. He argued that the melt-bearing seismic model of Weber et al. (2011) would require more than $\sim 1\%$ of melt and that retaining such an amount of melt would be difficult due to efficient compaction. Regarding the frequency-dependence of Q, Karato (2013) rejected the models of Efroimsky (2012a) and Nimmo et al. (2012) and suggested that the negative exponent p might be caused by non-linear anelasticity of the monthly tide and linear anelasticity of the annual tide. However, this idea was partly based on the incorrect assumption that the tide at the annual frequency is due to Sun-raised tidal deformation of the Moon. As explained by Williams et al. (2001), the annual modulation is produced by solar perturbations to lunar orbit only. The annual tide is thus raised by the Earth, just as the monthly tide. Still, the remark on a possible non-linearity of the lunar tide remains valid.

Adopting the density and rigidity profiles from a 10-layer structural model by Weber et al. (2011), Harada et al. (2014) explored the possible effects of a low-viscosity layer at the base of the mantle. To keep the number of unknowns reasonable, the authors set constant viscosity values for the lithosphere, mantle, low-viscosity layer, outer core, and inner core, and applied the Maxwell rheological model. They then calculated the tidal parameters for various thicknesses (outer radii 450–500 km) and viscosities (10^9–10^{21} Pa s) of the basal layer, at both the monthly and annual tidal frequencies, assuming that the rest of the mantle has a constant viscosity of $\eta = 10^{21}$ Pa s. With the highest considered basal layer thickness ($D_{\mathrm{LVZ}} = 170$ km) and a viscosity of about $2{\times}10^{16}$ Pa s, Harada et al. (2014) were able to reproduce the quality factors given by Williams et al. (2001) as well as their frequency dependence. Their value for the Love number at the monthly period falls into the interval $k_2 = 0.0242{\pm}0.0004$ suggested by Yan et al. (2012), while

their value of the Love number at the annual period fits into the interval $k_2 = 0.0255 \pm 0.0016$ observed by Goossens et al. (2011). Viscoelastic, the model of Harada et al. (2014) rendered different values of k_2 at the monthly and annual frequencies. This said, neither Yan et al. (2012) nor Goossens et al. (2011) considered frequency-dependence of their empirical values of k_2.

An updated version of the forward-modelling approach by Harada et al. (2014) was presented in Harada et al. (2016). Using the improved set of tidal parameters (limits on Q at four tidal frequencies and the values of k_2, k_3, and h_2 at the monthly frequency), the estimate of the basal layer's outer radius was expanded from 500 km to $540-560$ km (i.e., layer thickness $D_{\mathrm{LVZ}} = 210 - 230$ km for a core radius of 330 km) and the corresponding basal viscosity slightly changed to 3×10^{16} Pa s. In a recent follow-up study, Tan and Harada (2021) considered full radial profile of the lunar interior (Weber et al., 2011; Garcia et al., 2011) and assumed a temperature-dependent viscosity structure of the basal layer. The viscosity structure either followed a convective temperature profile (viscosity almost constant with depth) or a conductive profile (linear decrease of viscosity with depth). Since the former model was shown to match the selenodetic data better, the authors argued that the low-viscosity layer should be locally convecting. Moreover, they concluded that the layer's outer radius reaches 560 or 580 km (that is, to the depths of ~ 1160 km) and that the viscosity is the same as found by Harada et al. (2016).

The question whether a basal partial melt is required by the selenodetic data was also raised by Khan et al. (2014), though with an answer different from Nimmo et al. (2012). Khan et al. (2014) concentrated on detailed modelling of the lunar mantle petrology, and performed a Bayesian inversion of the mean density, the moment of inertia, the apparent resistivity, and the tidal data (k_2 and Q) at the monthly period. To model the tidal response of the lunar mantle within a purely elastic model, they calculated an anelastic correction to k_2 based on a homogeneous spherical model and the power-law dependence of tidal dissipation, which is valid for large *seismic* quality factors (or weak seismic wave attenuation; Zharkov & Gudkova, 2005). For cases with the Andrade parameter $\alpha > 0.1$, the resulting elastic k_2 clearly implied the existence of a partial melt in a basal layer with the thickness of $150-200$ km (i.e., a depth range $\sim 1250-1400$ km or the outer radii between ∼340-490 km). Khan et al. (2014) also found that, in order to be neutrally buoyant, the partially molten material should be enriched in FeO and TiO_2 with respect to the bulk mantle. In addition to the models with a partially molten layer, the authors tested a model with a fully solid mantle: this model still fitted all observations, except for the anelastically-corrected k_2.

Similarly, Matsumoto et al. (2015) performed a Bayesian inversion of seismic travel times and a set of available selenodetic data (mean density, moment of inertia, k_2, and Q at the monthly and annual frequencies), to infer the interior structure of an eight-layered lunar model. As in Harada et al. (2014), the authors considered the Maxwell rheological model, in which the existence of a low-viscosity layer is required not only by the slope of Q's frequency dependence but also by the magnitude of k_2. The viscosity of the solid mantle was always set to 10^{21} Pa s; otherwise, Matsumoto et al. (2015) varied a wide range of parameters. While their inverted structure of the shallow mantle agrees with the results of Weber et al. (2011) and Garcia et al. (2011), the lower mantle, mainly constrained by selenodetic data, slightly differs from the melt-containing model of Weber et al. (2011). The outer radius of the highly dissipative layer is around 570 km and the predicted viscosity in that region reaches $2.5^{+1.5}_{-0.9}\times10^{16}$ Pa s. The authors noted that with the model used, k_2 and the annual Q are slightly biased from the observed values, although not beyond 1σ. Matsumoto et al. (2015) also reported a trade-off between the outer core radius and the LVZ thickness. The thickness of the LVZ corresponding to the calculated outer radius is at least 170 km and, for the core size estimate of Weber et al. (2011), it may reach 240 km.

In a paper presenting their interpretation of LLR data, Williams and Boggs (2015) compared several rheological models and endeavoured to fit the lunar k_2/Q at the monthly

and annual tidal periods, considering physical libration at five periods (1 month, 206 days, 1 year, 3 years, and 6 years). Aware of the complex properties of the lunar interior and the possible unmodelled effects of its lateral heterogeneity, the authors proposed a model consisting of an absorption band and a narrow Debye peak: the former characterising the dissipation in the solid mantle, the latter describing the contribution of the partially molten layer suggested by Harada et al. (2014). For the thickness of the partially molten layer, Williams and Boggs (2015) obtained $D_{\mathrm{LVZ}} \geq 205\,\mathrm{km}$, placing its outer radius at $\geq 535\,\mathrm{km}$.

The results of Williams and Boggs (2015) are relatively consistent with the predictions by Harada et al. (2014); Matsumoto et al. (2015), and Harada et al. (2016). As in the other studies containing a LVZ, they indicate that if partial melt is present, it might extend to the zone of deep moonquakes. On the one hand, the coexistence of partially molten material with seismic sources is hard to imagine: while the former requires that the lower-mantle temperatures exceed solidus, the latter should be concentrated in regions where the mantle rocks undergo brittle deformation, limited to lower temperatures. On the other hand, the movement of small amounts of melt to the zone of moonquake nests might be considered one of the mechanisms triggering seismic events. Frohlich and Nakamura (2009) proposed an explanation for the periodic occurrence of deep moonquakes, which combines dehydration embrittlement due to partial melting and crack opening by moving fluids. The authors pointed out the correlation between tidal loading and seismic events associated with magma movements in terrestrial volcanoes and remarked that a similar process may be active in the lunar interior. Tentative evidence for a link between deep moonquakes and magma movements might also be seen in the correlation between the locations of deep moonquake nests and lunar maria (Qin et al., 2012). However, a definitive answer to the question of whether a rheologically weak layer and seismic sources can exist at comparable depths awaits further modelling efforts.

The specific effect of a partially-molten basal layer on the *elastic* Love number $k_{2,e}$ was discussed in the study of Raevskiy et al. (2015), which combined seismic and geodetic data with models of lunar mantle composition. Depending on the model used, the rigidity of the basal layer was required to be 20–50% lower than the rigidity of the overlying solid mantle and the outer radius of that zone was determined to reach 530–550 km. From the petrological perspective, the authors argued that partial melting of a peridotite/harzburgite mantle above the core-mantle boundary (CMB) would require temperatures in the depth of 1000 km to be in the range of 1350–1400 °C, unless the temperature gradients in the lower mantle become steeper. Furthermore, they concluded that the seismic velocities of Weber et al. (2011) are inconsistent with temperature profiles approaching solidus at the CMB. Although the models of Raevskiy et al. (2015) assume elastic response of the Moon, the authors also mentioned that anelasticity might explain the observed Love number without the need for a basal semi-molten layer.

Matsuyama et al. (2016) constrained their lunar interior models by the elastic Love numbers k_2 and h_2 (calculated using the same anelastic correction for Q at the monthly period as in Khan et al., 2014), the mean density of the Moon, and the moment of inertia. After carrying out MCMC-type inversion, the authors concluded that although the chosen observables do not rule out the existence of a semi-molten layer, there is a strong preference for higher, solid-mantle-like values of the lower-mantle rigidity. If the semi-molten layer exists, its thickness calculated by Matsuyama et al. (2016) is $D_{\mathrm{LVZ}} = 194^{+66}_{-186}\,\mathrm{km}$, its rigidity is $\mu_{\mathrm{LVZ}} = 43^{+26}_{-9}\,\mathrm{GPa}$, and its density may reach exceptionally high values, $\rho_{\mathrm{LVZ}} = 4676^{+410}_{-1179}\,\mathrm{kg\,m^{-3}}$.

Recently, the combined geochemical, seismic, and selenogetic ensemble of Raevskiy et al. (2015) was further studied by Kronrod et al. (2022), who extended the former work by considering explicitly a viscoelastic lunar interior. Regarding the division into interior layers and the adopted rheological model, the authors followed Matsumoto et al. (2015); i.e., they assumed the Maxwell model for the mantle and included a semi-molten basal

layer. Besides the main results of their Bayesian analysis, indicating a major difference in the chemical composition of the bulk silicate Earth and the Moon, Kronrod et al. (2022) presented probability distributions for the seismic wave velocities, mean density, and the thickness of the basal layer. The resulting distributions are wide, constraining the basal layer's density to 3400–3800 kg m^{-3} and the thickness to 100–350 km, depending on the mantle composition. As in Khan et al. (2014), the authors conclude that the layer should be enriched in TiO_2 and FeO, if it is present.

In summary, the literature discussing the unexpected frequency dependence of lunar tidal Q as well as the properties of a hypothetical semi-molten layer atop the lunar core is rich, and the proposed values of the layer's thickness range from 0 to 350 km. Models considering linear viscoelastic Maxwell rheology (both for the basal layer and for the bulk mantle; Harada et al., 2014, 2016; Matsumoto et al., 2015; Tan & Harada, 2021) typically arrive at viscosities of order 10^{16} Pa s. If the semi-molten layer exists, its upper radius extends to the depths of ~ 1150 km, i.e., just below the regions that are relatively well mapped by seismological studies and contain the nests of tidally-triggered deep moonquakes. Nevertheless, the existence of a low-viscosity layer is not necessarily required by selenodetic measurements at the best accessible, monthly period (Nimmo et al., 2012; Matsuyama et al., 2016). The main advantage of melt-bearing models lies in their ability to explain the possible increase in tidal Q from the monthly to the annual period.

2.3 Lunar k_2 and Q

Here, we shall use the potential tidal Love number derived from the GRAIL mission tracking data. Two independent analyses performed by the JPL group (Konopliv et al., 2013, the GL0660B solution) and the GSFC group (Lemoine et al., 2013, the GRGM660PRIM solution) yielded two possible values of the parameter: $k_2 = 0.02405 \pm 0.000176$ and $k_2 = 0.02427 \pm 0.00026$, respectively. The unweighted mean of the two alternative values is $k_2 = 0.02416 \pm 0.000222$ for a reference radius of 1738 km, and $k_2 = 0.02422 \pm 0.000222$ for the actual mean radius of 1737.151 km (Williams et al., 2014). For comparison, the recent analysis of the data from the Chang'e 5T1 mission gives $k_2 = 0.02430 \pm 0.0001$ (Yan et al., 2020). We note that the value obtained from satellite tracking data corresponds, in particular, to the real part of the complex Love number introduced later in Subsection 4.1. The GRAIL data are dominated by data arcs collected throughout a one-month time interval, and the resulting k_2 is thus interpreted as indicative of the deformation at monthly frequency (A. Konopliv, private communication).

The tidal quality factor Q was obtained by fitting tidal contribution to lunar physical libration measured by LLR (Williams et al., 2001, 2014; Williams & Boggs, 2015). Interpreting the measurements of physical libration presents a highly complex problem, depending on cross interactions of tides raised by the Earth and the Sun, precise modeling of the lunar orbit and of the instantaneous positions of the Earth-based stations and the Moon-based retroreflectors, and on an adequate incorporation of the lunar core-mantle friction (Williams et al., 2001). In practice, the tidal time delay at a monthly period and the dissipation-related corrections to the periodic latitudinal and longitudinal variations in the Moon's orientation are outputted and related analytically to linear combinations of k_2/Q at a number of loading frequencies. Since many of the loading frequencies are close to each other, the periodic corrections enable approximate estimation of the leading dissipation terms. Specifically, the strongest correction (compared to its uncertainty) is related to the annual longitudinal libration. Assuming a fixed k_2 at the monthly frequency, equal to the above-mentioned unweighted average, and using a complex rheological model best fitting the dissipation-related corrections to libration angles, Williams and Boggs (2015) derived the following frequency-dependent values of tidal quality factor: $Q = 38 \pm 4$ at the period of 1 month, $Q = 41 \pm 9$ at 1 year, and lower bounds of $Q \geq 74$ at 3 years and $Q \geq 58$ at 6 years. The tidal quality factors at other than the monthly frequency are model-dependent because the actual quantities extracted from

the dissipation-related corrections to libration angles are the ratios $(k_2/Q)_\chi/(k_2/Q)_{\rm monthly}$, where χ denotes frequency.

Williams and Boggs (2015) also attempted to find the frequency-dependence of k_2; however, the effect could not be detected by existing measurements. We note that in contrast to the unexpected frequency dependence of Q found with the JPL-based software (Williams et al., 2001, 2014; Williams & Boggs, 2015), an independent implementation of the fitting tool with different preset solutions for part of the geophysical phenomena (Pavlov et al., 2016) predicted $Q = 45$ at both the monthly and the annual frequencies.

As an additional, though a relatively weak constraint on the lunar interior structure, we consider the degree-3 potential tidal Love number k_3 and the degree-2 deformational Love number h_2 corresponding to radial deformation. The former has been derived from GRAIL mission tracking data and, as with k_2 above, we adopt the unweighted average of the two existing independent solutions (Lemoine et al., 2013; Konopliv et al., 2013): $k_3 = 0.0081 \pm 0.0018$. The latter has been measured by LLR and by laser altimetry (Mazarico et al., 2014; Pavlov et al., 2016; Viswanathan et al., 2018; Thor et al., 2021), the most recent value, presented by Thor et al. (2021), being $h_2 = 0.0387 \pm 0.0025$.

We would finally mention the reason why the constraints on the lunar interior from the measurements of k_3 are weak. A degree-l component of the internal tidal potential is proportional to r^l, where r is the distance between the centres of mass of the tidally perturbed body and the perturber. For this reason, with increasing degree l, the shallower depths contribute more and more to the Love numbers k_l. The sensitivity of the higher-degree Love numbers to the deep interior is, therefore, limited as compared to degree 2.

2.4 Outline of This Work

After an overview of the models and interpretations proposed in recent literature (with the focus on the last ten years of the discussion), we are ready to continue with the central part of this project. Our plan is to provide an interpretation of the unexpected frequency dependence of tidal Q which does not require partial melting (in a way similar to Nimmo et al., 2012) and compare it with a model containing a highly dissipative basal layer (Harada et al., 2014; Matsumoto et al., 2015). Section 3 introduces and gives a justification for the rheological model employed. Namely, it discusses the Sundberg-Cooper extension of the Andrade model and the dissipation related to elastically accommodated grain-boundary sliding (GBS). The following Section 4 links the non-elastic rheology to Love numbers and tidal quality factors. In Section 5, we first illustrate the expected position of a secondary peak in the dissipation spectrum of a homogeneous Moon, and then attempt to find the parameters of two- or three-layered lunar models that would produce the values of the monthly tidal Q and annual k_2/Q reported by Williams and Boggs (2015). At the same time, we fit the empirical values of lunar k_2, k_3, and h_2 given in Subsection 2.3. Section 6 discusses implication of both our models, and the results are briefly summarised in Section 7.

3 General Facts on Rheologies

3.1 Constitutive Equation

Rheological properties of a material are encoded in a constitutive equation interconnecting the present-time deviatoric strain tensor $u_{\gamma\nu}(t)$ with the values that have been assumed by the deviatoric stress $\sigma_{\gamma\nu}(t')$ over the time period $t' \leq t$. Under lin-

ear deformation, the equation has the form of convolution, in the time domain:

$$2\,u_{\gamma\nu}(t) \;=\; \hat{J}(t)\;\sigma_{\gamma\nu} \;=\; \int_{-\infty}^{t} \dot{J}\;(t-t')\;\sigma_{\gamma\nu}(t')\,dt' \quad , \tag{1}$$

and the form of product, in the frequency domain:

$$2\;\bar{u}_{\gamma\nu}(\chi) \;=\; \bar{J}(\chi)\;\bar{\sigma}_{\gamma\nu}(\chi) \quad . \tag{2}$$

Here $\bar{u}_{\gamma\nu}(\chi)$ and $\bar{\sigma}_{\gamma\nu}(\chi)$ are the Fourier images of strain and stress, while the complex compliance $\bar{J}(\chi)$ is a Fourier image of the kernel $\dot{J}(t-t')$ of the integral operator (1), see, e.g., Efroimsky (2012a, 2012b) for details.

3.2 The Maxwell and Andrade Models

At low frequencies, deformation of most minerals is viscoelastic and obeys the Maxwell model:

$$\dot{\mathbb{U}} = \frac{1}{2\,\mu}\;\dot{\mathbb{S}} + \frac{1}{2\,\eta}\,\mathbb{S} \tag{3a}$$

or, equivalently:

$$\dot{\mathbb{S}} + \frac{1}{\tau_{\rm M}}\,\mathbb{S} \;=\; 2\,\mu\;\dot{\mathbb{U}} \quad , \tag{3b}$$

$\mathbb{U}$ and $\mathbb{S}$ being the deviatoric strain and stress; η and μ denoting the viscosity and rigidity. (Below, we shall address the question as to whether μ is the unrelaxed or relaxed rigidity.) The *Maxwell time* is introduced as

$$\tau_{\rm M} \;\equiv\; \frac{\eta}{\mu} \quad . \tag{4}$$

For this rheological model, the kernel of the convolution operator (1) is a time derivative of the compliance function

$$^{(M)}J(t\,-\,t') \;=\; \left[\,J_{\rm e}\,+\,(t\,-\,t')\;\frac{1}{\eta}\,\right]\;\Theta(t\,-\,t') \quad , \tag{5}$$

where $\Theta(t-t')$ is the Heaviside step function, while the elastic compliance $J_{\rm e}$ is the inverse of the shear rigidity μ:

$$J_{\rm e} \;\equiv\; \frac{1}{\mu} \quad . \tag{6}$$

In the frequency domain, equation (3) can be cast into form (2), with the complex compliance given by

$$^{(M)}\bar{J}\,(\chi) \;=\; J_e\,-\,\frac{i}{\eta\chi} \;=\; J_{\rm e}\left(1\,-\,\frac{i}{\chi\,\tau_{\rm M}}\right) \quad , \tag{7}$$

and the terms $J_{\rm e}$ and $-\,i/(\eta\chi)$ being the elastic and viscous parts of deformation, correspondingly. So a Maxwell material is elastic at high frequencies, viscous at low.

More general is the combined Maxwell-Andrade rheology, often referred to simply as the Andrade rheology. It comprises inputs from elasticity, viscosity, and anelastic processes:

$$^{(A)}J(t) = J_{\rm e} + \beta\,t^{\alpha} + \frac{t}{\eta} \quad , \tag{8}$$

the corresponding complex compliance being

$$^{(A)}\bar{J}\,(\chi) \;=\; J_{\rm e} \,+\, \beta\,(i\chi)^{-\alpha}\,\Gamma\,(1+\alpha) \,-\, \frac{i}{\eta\chi} \tag{9a}$$

$$\;=\; J_{\rm e} \,+\, \beta\,(i\chi)^{-\alpha}\,\Gamma\,(1+\alpha) \,-\, i\,J\,(\chi\,\tau_{\rm M})^{-1} \quad , \tag{9b}$$

where Γ is the Gamma function, while α and β denote the dimensionless and dimensional Andrade parameters.

Expressions (9a - 9b) suffer an inconvenient feature, the fractional dimensions of the parameter β. It was therefore suggested in Efroimsky (2012a, 2012b) to shape the compliance into a more suitable form

$$ {}^{(A)}J(t) = J_{\rm e}\left[1 + \left(\frac{t}{\tau_{\rm A}}\right)^{\alpha} + \frac{t}{\tau_{\rm M}}\right]\Theta(t - t') \ , \tag{10} $$

$$ {}^{(A)}\bar{J}(\chi) \ = \ J_{\rm e}\left[1 + (i\,\chi\,\tau_{\rm A})^{-\alpha}\,\Gamma(1+\alpha) \ - \ i\,(\chi\,\tau_{\rm M})^{-1}\right] \ , \tag{11} $$

with the parameter τ_A christened as *the Andrade time* and linked to β through

$$ \beta \ = \ J_{\rm e}\ \tau_{\rm A}^{-\alpha} \ \ . \tag{12} $$

Compliance (11) is identical to (9a) and (9b), but is spared of the parameter β of fractional dimensions.

3.3 Why the Maxwell and Andrade Models Require Refinement

In the literature, it is common to postulate that both the rigidity and compliance assume their *unrelaxed* values denoted with $\mu_{\rm U}$ and $J_{\rm U}$.

This convention is reasonable for sufficiently high frequencies:

$$ \chi \ \text{ is high} \qquad \Longrightarrow \qquad \mu \ = \ \mu_{\rm U} \qquad \text{and} \qquad J_{\rm e} \ = \ J_{\rm U} \ \ . \tag{13} $$

The convention, however, becomes unjustified for low frequencies. In that situation, the material has, at each loading cycle, enough time to relax, wherefore both the rigidity modulus and its inverse assume values different from the unrelaxed ones. In the zero-frequency limit, they must acquire the relaxed values:

$$ \chi \ \to \ 0 \qquad \Longrightarrow \qquad \mu \ \to \ \mu_{\rm R} \qquad \text{and} \qquad J_{\rm e} \ \to \ J_{\rm R} \ \ . \tag{14} $$

This fact must be taken care of, both within the Maxwell and Andrade models.

3.4 Generalisation of the Maxwell and Andrade Models, According to Sundberg and Cooper (2010)

The simplest expression for the time relaxation of the elastic part of the compliance is

$$ J_{\rm e}(t) \ = \ J_{\rm U} \ + \ (J_{\rm R} \ - \ J_{\rm U})\left[1 \ - \ e^{-t/\tau}\right] \tag{15a} $$

$$ = \ J_{\rm U}\left[1 \ + \ \Delta\left(1 - e^{-\,t/\tau}\right)\right] \ , \tag{15b} $$

where the so-called relaxation strength is introduced as

$$ \Delta \equiv \frac{J_{\rm R}}{J_{\rm U}} - 1 \ \ , \tag{16} $$

while τ is the characteristic relaxation time. When relaxation of $J_{\rm e}$ is due to elastically accommodated grain-boundary sliding, this time can be calculated as

$$ \tau \ = \ \tau_{\rm gbs} \ = \ \frac{\eta_{\rm gb}\,d}{\mu_{\rm U}\,\delta} \ , \tag{17} $$

where $\eta_{\rm gb}$ is the grain-boundary viscosity, d is the grain size, while δ is the structural width of the grain boundary.

In the frequency domain, this compliance writes as

$$\bar{J}_{\rm e}(\chi) \;=\; J_{\rm U}\left[1 \;+\; \frac{\Delta}{1 \,+\, \chi^2\,\tau^2} \;+\; i\,\frac{\chi\,\tau\,\Delta}{1 \,+\, \chi^2\,\tau^2}\right] \;, \tag{18}$$

its imaginary part demonstrating a Debye peak. Our goal is to trace how this Debye peak translates into the frequency-dependence of the inverse tidal quality factor $1/Q$ and of k_2/Q of a near-spherical celestial body.

Substitution of formula (18) into the overall expression (11) for the Andrade complex compliance will produce the Sundberg and Cooper (2010) compliance:

$$\bar{J}\,(\chi) \;\;=\;\; J_{\rm U}\left[1+\frac{\Delta}{1+\chi^2\tau^2} \;-\; i\,\frac{\chi\,\tau\,\Delta}{1+\chi^2\tau^2} + (i\chi\tau_{\rm A})^{-\alpha}\,\Gamma(1+\alpha) - i(\chi\tau_{\rm M})^{-1}\right] \tag{19a}$$

$$\;\;=\;\; J_{\rm U}\left[1 \;+\; \frac{\Delta}{1 \,+\, \chi^2\,\tau^2} \;+\; \Gamma(1+\alpha)\,\zeta^{-\alpha}\,(\chi\tau_{\rm M})^{-\alpha}\,\cos\left(\frac{\alpha\pi}{2}\right)\right] \tag{19b}$$

$$-\;\; i\,J_{\rm U}\left[\frac{\chi\,\tau\,\Delta}{1 \,+\, \chi^2\,\tau^2} \;+\; \Gamma(1+\alpha)\,\zeta^{-\alpha}\,(\chi\tau_{\rm M})^{-\alpha}\,\sin\left(\frac{\alpha\pi}{2}\right) \;+\; (\chi\tau_{\rm M})^{-1}\right] \;,$$

where we introduced the dimensionless Andrade time

$$\zeta \;=\; \frac{\tau_{\rm A}}{\tau_{\rm M}} \quad . \tag{20}$$

Be mindful that in expression (10) it is only the first term, $J_{\rm e}$, that is changed to function (15b). Accordingly, in equation (11), it is only the first term, $J_{\rm e}$, that is substituted with function (18). In the other terms, both the Maxwell and Andrade times are still introduced through the unrelaxed value $J_{\rm e} = J_{\rm U}$:

$$\tau_{\rm M} \;\equiv\; \eta\,J_{\rm U} \;\;,\;\;\; \tau_{\rm A} \;\equiv\; \left(\frac{J_{\rm U}}{\beta}\right)^{1/\alpha} \quad . \tag{21}$$

Had we combined the elastic relaxation rule (18) with the Maxwell model (7) instead of Andrade, we would have arrived at the Burgers model — which would be equation (19) with the Andrade terms omitted, i.e. with $\tau_{\rm A} \longrightarrow \infty$. Simply speaking, in the absence of transient processes, Andrade becomes Maxwell, while Sundberg-Cooper becomes Burgers.

Along with the dimensionless Andrade time ζ, we shall employ below the relative relaxation time

$$t_{\rm rel} = \frac{\tau}{\tau_{\rm M}} \tag{22}$$

relating the relaxation timescale for the compliance $J_{\rm e}$ to the Maxwell time.

3.5 Further Options

The characteristic relaxation time τ can be replaced with a distribution $D(\tau)$ of times spanning an interval from a lower bound $\tau_{\rm L}$ to an upper bound $\tau_{\rm H}$. So the relaxation of the elastic part of the compliance will be not

$$J_{\rm e}(t) \;=\; J_{\rm U}\,\left[1 \;+\; \Delta\,\left(1 - e^{-\,t/\tau}\right)\right] \tag{23}$$

but

$$J_e(t) = J_U\left[1 + \Delta\int_{\tau_L}^{\tau_H} D(\tau)\left[1 - \exp\left(-\,\frac{t}{\tau}\right)\right]d\tau\right] \quad . \tag{24}$$

If the relaxation is due to elastically-accommodated GBS, this distribution would be a consequence of variable grain-boundary viscosity, grain sizes and shapes, and non-uniform

orientation of grain boundaries with respect to the applied stress (see also Lee & Morris, 2010).

Insertion of expression (24) in the Maxwell model (5) or in the Andrade model (10) produces the *extended Burgers model* or the *extended Sundberg-Cooper model*, correspondingly. For details, see Bagheri et al. (2022) and references therein.

4 Complex Love Numbers and Quality Functions

The perturbing potential wherewith the Earth is acting on the Moon can be decomposed in series over Fourier modes ω_{lmpq} parameterised with four integers $lmpq$. If the tidal response of the Moon is linear, both the produced deformation and the resulting additional tidal potential of the Moon are expandable over the same Fourier modes, as proved in Efroimsky and Makarov (2014, Appendix C). The proof is based on the fact that a linear integral operator (convolution) in the time domain corresponds to a product of Fourier images in the frequency domain.

While the Fourier modes can be of either sign, the physical forcing frequencies in the body are

$$\chi_{lmpq} \;=\; |\omega_{lmpq}| \;. \tag{25}$$

An extended discussion of this fact can be found in Section 4.3 of Efroimsky and Makarov (2013).

Wherever this causes no confusion, we omit the subscript to simplify the notation:

$$\omega \equiv \omega_{lmpq} \quad , \quad \chi \equiv \chi_{lmpq} \;. \tag{26}$$

4.1 The Complex Love Number

Writing the degree-l complex Love number as

$$\bar{k}_l(\omega) \;=\; \Re\left[\bar{k}_l(\omega)\right] \;+\; i\,\Im\left[\bar{k}_l(\omega)\right] \;=\; |\bar{k}_l(\omega)|\, e^{\,-i\epsilon_l(\omega)} \quad , \tag{27}$$

we conventionally denote the phase as $-\epsilon_l$, with a "minus" sign. This convention imparts ϵ_l with the meaning of phase lag. We also introduce the so-called *dynamical Love number*

$$k_l(\omega) \;=\; |\bar{k}_l(\omega)| \;. \tag{28}$$

A key role in the tidal theory is played by the *quality functions*

$$K_l(\omega) \;\equiv\; -\,\Im\left[\,\bar{k}_l(\omega)\,\right] \;=\; \bar{k}_l(\omega)\,\sin\epsilon_l(\omega) \tag{29a}$$

entering the series expansions for tidal forces, torques, dissipation rate (Efroimsky & Makarov, 2014), and orbital evolution (Boué & Efroimsky, 2019)

Since $\mathrm{Sign}\,\epsilon_l(\omega) = \mathrm{Sign}\,\omega$ (Efroimsky & Makarov, 2013), they can be written as

$$K_l(\omega) \;\equiv\; -\,\Im\left[\,\bar{k}_l(\omega)\,\right] \;=\; \frac{k_l(\omega)}{Q_l(\omega)}\;\mathrm{Sign}\,\omega \quad , \tag{29b}$$

where the tidal quality factor is introduced via

$$Q_l^{-1}(\omega) \;=\; |\,\sin\epsilon_l(\omega)\,| \;. \tag{30}$$

The dependency $\sin\epsilon_l(\omega)$ being odd, the function $Q_l(\omega)$ is even. Also, even is the function $k_l(\omega)$. Therefore, for any sign of ω and ϵ_l, it is always possible to treat both $Q_l(\omega)$ and $k_l(\omega)$ as functions of the forcing frequency $\chi \equiv |\omega|$:

$$Q_l(\omega) \;=\; Q_l(\chi) \quad , \quad k_l(\omega) \;=\; k_l(\chi) \quad . \tag{31}$$

Often attributed to Biot (1954), though known yet to Sir George Darwin (1879), the so-called *correspondence principle*, or the *elastic-viscoelastic analogy*, is a valuable key to numerous problems of viscoelasticity. It enables one to derive solutions to these problems from the known solutions to analogous static problems. In application to bodily tides, this principle says that the complex Love number of a uniform spherical viscoelastic body, $\bar{k}_l(\chi)$, is linked to the complex compliance $\bar{J}(\chi)$ by the same algebraic expression through which the static Love number k_l of that body is linked to the relaxed compliance $J_{\rm R}$:

$$\bar{k}_l(\chi) \;=\; \frac{3}{2\,(l\,-\,1)}\;\frac{1}{1\,+\,\mathcal{B}_l/\bar{J}(\chi)} \quad , \tag{32}$$

where

$$\mathcal{B}_l \;\equiv\; \frac{(2\,l^{\,2}\,+\,4\,l\,+\,3)}{l\,g\,\rho\,R} \;=\; \frac{3\,(2\,l^{\,2}\,+\,4\,l\,+\,3)}{4\;l\,\pi\,G\,\rho^2\,R^2} \quad , \tag{33}$$

ρ, R, and g being the density, radius, and surface gravity of the body, and G being Newton's gravitational constant.

As an aside, we would mention that while $-\Im\,[k_l(\omega)]$ emerges in the tidal torque, the real part of the complex Love number, $\Re\,[k_l(\omega)] = k_l(\omega)\,\cos\epsilon_l(\omega)$, shows up in the expansion for the tidal potential. Not considered further in the present study, the general expression for this product and its version for the Maxwell and other rheologies can be found in Efroimsky (2015, Appendix A6).

4.2 $k_l(\chi)/Q_l(\chi)$ and $1/Q_l(\chi)$ for an Arbitrary Rheology

Expression (32) entails:

$$K_l(\chi) \;=\; k_l(\chi)\;\sin\epsilon_l(\chi) \;=\; -\;\frac{3}{2(l-1)}\;\frac{\mathcal{B}_l\;\Im\left[\bar{J}(\chi)\right]}{\left(\Re\left[\bar{J}(\chi)\right]+\mathcal{B}_l\right)^2+\left(\Im\left[\bar{J}(\chi)\right]\right)^2} \quad , \tag{34}$$

the coefficients $\mathcal{B}_l$ rendered by equation (33). We see that for a homogeneous incompressible sphere, the information needed to calculate the quality function comprises the radius, the density, and the rheological law $\bar{J}(\chi)$.

The inverse tidal quality factor of degree l is given by (Efroimsky, 2015)

$$Q_l(\chi)^{-1} \equiv\; |\,\sin\epsilon_l(\chi)\,| \;\;, \tag{35}$$

$$\sin\epsilon_l(\chi) \;=\; -\;\frac{\mathcal{B}_l\;\;\Im\left[\bar{J}(\chi)\right]}{\sqrt{\left(\,\Re\left[\bar{J}(\chi)\right]\,\right)^2+\left(\,\Im\left[\bar{J}(\chi)\right]\,\right)^2}\;\sqrt{\left(\,\Re\left[\bar{J}(\chi)\right]+\mathcal{B}_l\right)^2+\left(\Im\left[\bar{J}(\chi)\right]\right)^2}} \quad . \tag{36}$$

All new is well-forgotten old. As we were writing this paper, it became known to us that for the Maxwell rheology the frequency-dependence of $\sin\epsilon_2$ was studied yet by Gerstenkorn (1967, Fig. 2) in a work that went virtually unnoticed. Because of different notation and Gerstenkorn's terse style, it is not apparent if his values for the peak's magnitude and location are the same as ours. However, the overall shape of the frequency-dependence of $\sin\epsilon_2$ obtained by Gerstenkorn (1967) seems right.

4.3 Notational Point: Q and Q_2

In publications where both seismic and tidal dissipation are considered, it is necessary to distinguish between the seismic and tidal quality factors. In that situation, the letter Q without a subscript is preserved for the seismic factor.

In the literature on tides, it is common to employ Q as a shorter notation for the quadrupole tidal factor Q_2. We shall follow the latter convention:

$$Q \;\equiv\; Q_2 \;\;, \tag{37}$$

and shall use the two notations intermittently.

4.4 The frequency-dependencies of k_l/Q_l and $1/Q_l$ for the Maxwell and Andrade models

For a homogeneous sphere composed of a Maxwell or Andrade material, the quality function $K_l(\omega)$ has a kink form, as in Figure 1. The function $\sin\epsilon_l(\omega)$ is shaped similarly.

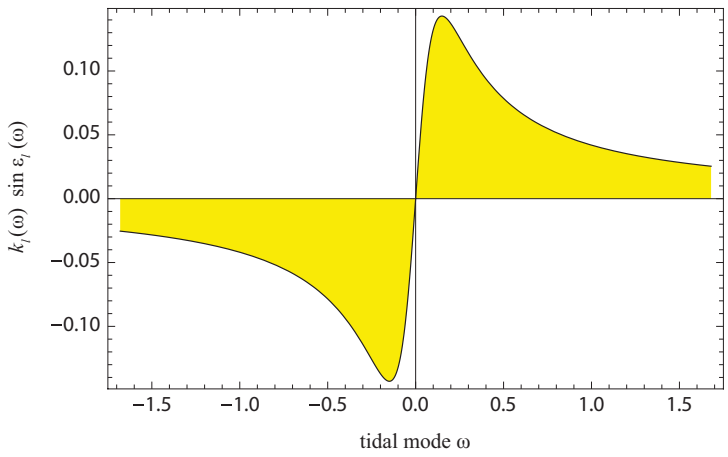

Figure 1. A typical shape of the quality function $K_l(\omega) = k_l(\omega)\sin\epsilon_l(\omega)$, where ω is a shortened notation for the tidal Fourier mode ω_{lmpq}. (From Noyelles et al., 2014).

Insertion of expression (7) into equation (34) shows that for a spherical Maxwell body the extrema of the kink $K_l(\omega)$ are located at

$$\omega_{\mathrm{peak}_l} = \pm \frac{\tau_{\mathrm{M}}^{-1}}{1+\mathcal{B}_l\,\mu} \tag{38}$$

the corresponding extrema assuming the values

$$K_l^{(\mathrm{peak})} = \pm \frac{3}{4(l-1)}\,\frac{\mathcal{B}_l\,\mu}{1+\mathcal{B}_l\,\mu}\ , \tag{39}$$

wherefrom $|K_l| < \frac{3}{4(l-1)}$.

Inside the interval between peaks, the quality functions are near-linear in ω:

$$|\omega| < |\omega_{\mathrm{peak}_l}| \quad\Longrightarrow\quad K_l(\omega) \simeq \frac{3}{2(l-1)}\,\frac{\mathcal{B}_l\,\mu}{1+\mathcal{B}_l\,\mu}\,\frac{\omega}{|\omega_{\mathrm{peak}_l}|}\ . \tag{40}$$

Outside the inter-peak interval, they fall off as about ω^{-1}:

$$|\omega| > |\omega_{\mathrm{peak}_l}| \quad\Longrightarrow\quad K_l(\omega) \simeq \frac{3}{2(l-1)}\,\frac{\mathcal{B}_l\,\mu}{1+\mathcal{B}_l\,\mu}\,\frac{|\omega_{\mathrm{peak}_l}|}{\omega}\ . \tag{41}$$

While the peak magnitudes (39) are ignorant of the viscosity η, the spread between the peaks scales as the inverse η, as evident from expression (38). The lower the mean viscosity, the higher the peak frequency $|\omega_{\mathrm{peak}_l}|$.

It can be demonstrated using equation (36) that for a homogeneous Maxwell body the extrema of $\sin\epsilon_l(\omega)$ are located at

$$\omega_{\text{peak of } \sin\epsilon_l} = \pm \frac{\tau_{\text{M}}^{-1}}{\sqrt{1+\mathcal{B}_l\mu}} \ . \tag{42}$$

For the Moon, this peak is located within a decade from its counterpart for K_l given by formula (38).

In many practical situations, only the quadrupole ($l=2$) terms matter. The corresponding peaks are located at

$$\omega_{\text{peak}_2} = \pm \frac{\tau_{\text{M}}^{-1}}{1+\mathcal{B}_2\,\mu} \approx \pm \frac{1}{\mathcal{B}_2\,\eta} = \pm \frac{8\,\pi\,G\,\rho^2\,R^2}{57\,\eta} \quad . \tag{43}$$

The approximation in this expression relies on the inequality $\mathcal{B}_l\,\mu \gg 1$, fulfilment whereof depends on the size of the body. For a Maxwell Moon with $\mu = 6.4\times10^{10}$ Pa and $G(\rho R)^2 \approx 2.24\times10^9$ Pa, we have $\mathcal{B}_2\,\mu \approx 64.5$, so the approximation works.

While for the Maxwell and Andrade models each of the functions $K_l(\omega)$ and $\sin\epsilon_l(\omega)$ possesses only one peak for a positive argument, the situation changes for bodies of a more complex rheology. For example, the existence of an additional peak is ensured by the insertion of the Sundberg-Cooper compliance (19) into expressions (34) or (36).

5 Application to the Moon

5.1 The "Wrong" Slope Interpreted with the Maxwell Model

As we explained in Section 1, fitting of the LLR-obtained quadrupole tidal quality factor $Q = Q_2$ to the power law $Q \sim \chi^p$ resulted in small negative value of the exponential p (Williams & Boggs, 2015). An earlier attempt to explain this phenomenon implied an identification of this slightly negative slope with the incline located to the left of the maximum of the quality function $(k_2/Q_2)(\chi)$, see Figure 1. Within this interpretation, $\chi_{\text{peak}} \equiv |\omega_{\text{peak}}|$ should be residing somewhere between the monthly and annual frequencies explored in Williams and Boggs (2015). As was explained in Efroimsky (2012a) , this sets the mean viscosity of the Moon as low as

$$\eta \approx 3\times10^{15} \text{ Pa s} \ , \tag{44}$$

The extrema of $(1/Q_2)(\chi)$ are close to those of $(k_2/Q_2)(\chi)$, as can be observed from equations (19) and (45) Efroimsky (2015). Therefore, had we used instead of the maximum of k_2/Q_2 given by (43) the maximum of $1/Q_2$ given by (42), the ensuing value would have been only an order higher:

$$\eta \approx 4\times10^{16} \text{ Pa s} \ . \tag{45}$$

Such values imply a high concentration of the partial melt in the mantle – quite in accordance with the seismological models by Nakamura et al. (1974) and Weber et al. (2011).

However, employment of a rheology more realistic than Maxwell may entail not so low a viscosity — in which case the existence of a semi-molten layer may be questioned.

5.2 Frequency Dependence of Tidal Dissipation in the Sundberg-Cooper Model

The Debye peak emerging in the imaginary part of $\bar{J}_{\text{e}}$ (equation (18)) will, obviously, show itself also in the shape of the imaginary part of the overall $\bar{J}$, the bottom line of equation (19b). Consequently, substitution of expression (19) in equations (34)

and (36) will entail the emergence of a Debye warp on the kinks for k_l/Q_l and $1/Q_l$. Where will the additional peak be located for realistic values of the relaxation timescale τ? What values for the mean viscosity will it entail?

In the end of Section 3.4, we introduced the relative relaxation time as $t_{\text{rel}} \equiv \tau/\tau_{\text{M}}$. Figure 2 illustrates specifically the effect of t_{rel} in the Sundberg-Cooper model on the position of the additional Debye peak for a homogeneous lunar interior with an arbitrarily chosen high mean viscosity $\eta_{\text{Moon}} = 10^{22}$ Pa s. The emergence of another local maximum in the k_2/Q_2 and $1/Q_2$ functions may naturally explain the decrease in dissipation (or increase in the quality factor Q) with frequency, even within a homogeneous and highly viscous model.

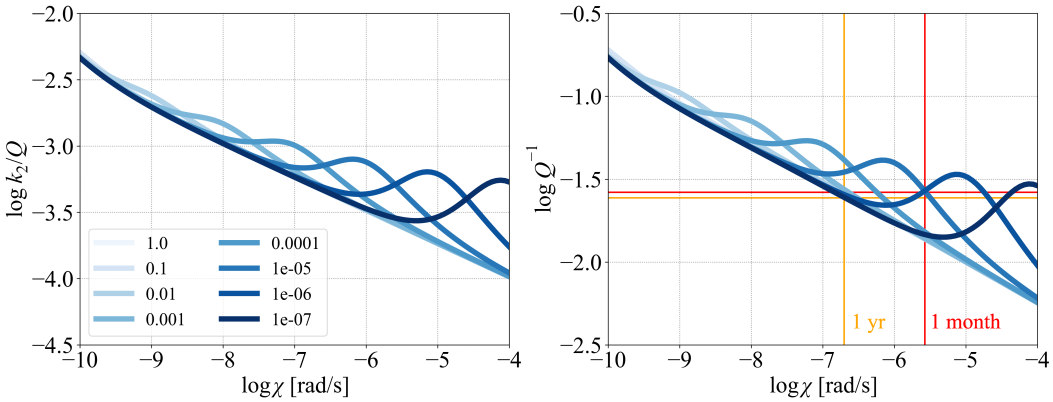

Figure 2. The negative imaginary part of the Love number (left) and the inverse quality factor (right) for different ratios between the timescale τ and the Maxwell time τ_{M} (indicated by the shades of blue). The yellow and red vertical lines show the Q_2 values given by Williams and Boggs (2015) for the annual and the monthly component, respectively. In this case, we consider a homogeneous lunar interior model governed by the Sundberg-Cooper rheology. The mantle viscosity was set to 10^{22} Pa s and the mantle rigidity to 80 GPa.

5.3 Constructing a Multi-layered Model

Section 4 introduced the complex Love number $\bar{k}_l(\chi)$ for an arbitrary linear anelastic or viscoelastic rheology assuming a homogeneous incompressible sphere. While such a model can reasonably approximate the response of the Moon with a homogeneous mantle and a small core (see also Figure 4), its application to a body with a highly dissipative basal layer would not be accurate (Bolmont et al., 2020). Planetary interior with a highly dissipative layer can still be approximated by a homogeneous model with an additional absorption peak or band in the underlying rheological law. However, we would need to know the mapping between the parameters of the dissipative layer and the parameters of the additional peak (Gevorgyan, 2021).

Therefore, in the following sections, we will complement the homogeneous model with three models consisting of two or three layers and we will calculate the corresponding complex Love numbers numerically, using a matrix method based on the normal mode theory (e.g., Takeuchi & Saito, 1972; Wu & Peltier, 1982; Sabadini & Vermeersen, 2004). For the sake of simplicity, we consider all layers in the numerical model (linearly) viscoelastic and we model the response of liquid layers by the Maxwell model with J_{e} in equation (7) approaching 0. This method has also been tested against another implementation of the same model, in which the liquid layers were inputted through differ-

ent boundary conditions; the results obtained within the two approaches are virtually the same. Using the outputted complex Love numbers for various rheological parameters, we then proceed by fitting the empirical values. If not stated differently for illustrative purposes, the three alternative models will always comprise a liquid core with a low viscosity ($\eta_c = 1\,\mathrm{Pa\,s}$), a constant density ($\rho_c = 5000\,\mathrm{kg\,m^{-3}}$), and an outer radius identical to the mean value reported by Weber et al. (2011), $R_c = 330\,\mathrm{km}$.

Although the existence of an inner core is possible and even indicated by the stacked seismograms presented by Weber et al. (2011), its response to tidal loading would be decoupled from the rest of the mantle, and it would contribute to the resulting tidal deformation only negligibly. Therefore, we do not include the inner core in our modelling.

Subsection 5.4 makes use of a two-layered model consisting of the liquid core and a homogeneous mantle, the response of which is described by the Andrade rheology. For the mantle density, we prescribe a constant value of $\rho_m = 3300\,\mathrm{kg\,m^{-3}}$, and Andrade parameter ζ is set to 1, implying comparable timescales for viscous and anelastic relaxation. Other values of ζ were also tested and their effect on the results is discussed in the aforementioned Subsection. The viscosity η_m, rigidity μ_m, and Andrade parameter α of the mantle are treated as free parameters and fitted to the data.

The second model, considered in Subsection 5.5, comprises a liquid core and a Sundberg-Cooper homogeneous mantle. The mantle density is always set to the average value $\rho_m = 3300\,\mathrm{kg\,m^{-3}}$. Rheological parameters η_m, μ_m, τ, and Δ are fitted, while the Andrade empirical parameters α and ζ are held constant during each run of the inversion. We have also tested the effect of varying α in the range $[0.1, 0.4]$ and of magnifying or reducing ζ by one order of magnitude.

The model with a basal dissipative layer, which is discussed in Subsection 5.6, contains a core and a two-layered mantle. Each layer of the mantle is assumed to be homogeneous. The basal layer is decribed by the Maxwell model with fitted parameters μ_{LVZ} and η_{LVZ}; additionally, we fit its outer radius R_{LVZ}. For the overlying bulk mantle, we consider the Andrade model with free (fitted) parameters η_m, μ_m and with α, ζ kept constant during each run of the inversion. Both mantle layers have a prescribed density of $\rho_{LVZ} = \rho_m = 3300\,\mathrm{kg\,m^{-3}}$. The reason for using the simple Maxwell model instead of the Andrade model in the basal layer is the following: in order to fit the measured tidal quality factor Q at the monthly and the annual frequency, the peak dissipation from the basal layer should be located either between these frequencies, or above the monthly frequency. At the same time, in the vicinity of the peak dissipation, the Andrade and Maxwell rheologies are almost indistinguishable from each other. (Comparing the last two terms on the final line of equation (19), we observe that the viscous term exceeds the Andrade term when $\tau_M \chi \ll (\tau_A/\tau_M)^{\alpha/(1-\alpha)}$. In realistic situations, $\tau_M \chi_{\mathrm{peak}}$ satisfies this condition safely. So, near the peak the Andrade term is virtually irrelevant, and the regime is almost Maxwell.) Hence, we chose the simpler of the two rheological models. This decision will also facilitate the comparison of our results for the basal layer's characteristics with the predictions by Harada et al. (2014, 2016), and Matsumoto et al. (2015), who likewise modeled the basal layer with the Maxwell model. In contrast to our study, they applied the same model to the mantle as well.

In this work, we are not predicting the mineralogy of the mantle — and the composition of the basal layer, if present, is only briefly discussed in Subsection 6.2. Our use of a homogeneous mantle layer (or two homogeneous mantle layers) reflects our lack of information on the exact chemical and mineralogical composition, the grain size, the thermal structure, and the presence of water. Instead, we characterise the mantle with a single, "effective", rigidity and viscosity, which can be later mapped to a detailed interior structure (see also Dumoulin et al., 2017; Bolmont et al., 2020, who discussed the effect of approximating a radially stratified mantle with a homogeneous one for Venus and terrestrial exoplanets). Furthermore, we neglect any lateral heterogeneities in the lunar interior. We also assume that the lunar mantle is incompressible and can be reasonably

755 described by a linear viscoelastic model — which is valid at low stresses. Given the mag-
756 nitude of tidal stresses in the Moon, this assumption might have to be lifted in future
757 works, though (Karato, 2013).

758 Since the radial structure of our models is deliberately simplified, we do not attempt
759 to fit either the mean density or the moment of inertia given for the Moon. (The mean
760 density of our lunar toy-models is less than 1% lower than the actual value.) The inver-
761 sions presented below are only performed for the tidal parameters, namely k_2 and tidal
762 Q at the monthly frequency, k_2/Q at the annual frequency, and k_3, h_2 at the monthly
763 frequency. A list of the model parameters in the reference cases discussed in the follow-
764 ing sections is presented in Table 1. The empirical values considered are then given in
765 Table 2.

Parameter	Type	Value	Unit
Common parameters			
Core size R_c	const.	330	km
Core viscosity η_c	const.	1	Pa s
Core density ρ_c	const.	$5,000$	kg m^{-3}
Mantle viscosity η_m	fitted	$10^{15} - 10^{30}$	Pa s
Mantle rigidity μ_m	fitted	$10^{9} - 10^{12}$	Pa
Mantle density ρ_m	const.	$3,300$	kg m^{-3}
Andrade parameter ζ	const.	1	—
Two-layered model I (Andrade mantle)			
Andrade parameter α	fitted	$0 - 0.5$	—
Two-layered model II (Sundberg-Cooper mantle)			
Andrade parameter α	const.	0.2	—
Relaxation strength Δ	fitted	$10^{-5} - 10^{0}$	—
Relative relaxation time t_rel	fitted	$10^{-7} - 10^{0}$	—
Three-layered model (Andrade mantle)			
Andrade parameter α	const.	0.2	—
Thickness of the basal layer D_LVZ	fitted	$0 - 370$	km
Viscosity of the basal layer η_LVZ	fitted	$10^{0} - 10^{30}$	Pa s
Rigidity of the basal layer μ_LVZ	fitted	$0 - \mu_\mathrm{m}$	Pa

Table 1. Parameters of the three models considered in this work.

766 ### 5.4 Applicability of the Andrade Model

767 Before discussing the two interior models able to fit the anomalous frequency de-
768 pendence of lunar tidal dissipation, we first attempt to use the full set of tidal param-
769 eters given in Table 2 to constrain a simpler model, which only contains a liquid core and
770 a viscoelastic mantle governed by the Andrade rheology (equation (11)). Such a model,
771 accounting neither for a basal dissipative layer nor for elastically-accommodated GBS,
772 might still be able to fit the data. Thanks to the large uncertainty on the lunar qual-
773 ity factor (more than 10% at the monthly frequency and 20% at the annual frequency,
774 Williams & Boggs, 2015), we may not need to introduce any additional complexities to
775 interpret the tidal response of the Moon. The error bars of the tidal quality factors are
776 so wide that they allow, at least in principle, for a situation where $Q_{2,\,\mathrm{annual}}$ is smaller
777 than $Q_{2,\,\mathrm{monthly}}$.

Parameter	Value	Reference
k_2, monthly	0.02422 ± 0.00022	Williams et al. (2014)
Q, monthly[a]	38 ± 4	Williams and Boggs (2015)
k_2/Q, annual[a]	$(6.2 \pm 1.4) \times 10^{-4}$	Williams and Boggs (2015)
k_3, monthly[b]	0.0081 ± 0.0018	Konopliv et al. (2013); Lemoine et al. (2013)
h_2, monthly	0.0387 ± 0.0025	Thor et al. (2021)

[a] The standard deviations from this table are only used in Subsection 5.4. In the rest of the paper, we arbitrarily set the uncertainties to 1% of the mean value. [b] Listed is the unweighted mean of the values given in references.

Table 2. Observational constraints used in this work.

To find the parameters of this preliminary model, we performed a Bayesian inversion using the MCMC approach and assuming Gaussian distribution of observational uncertainties (e.g., Mosegaard & Tarantola, 1995). In particular, we employed the *emcee* library for *Python* (Foreman-Mackey et al., 2013), which is based on the sampling methods proposed by Goodman and Weare (2010). The algorithm was instructed to look for the mantle viscosity η_m, the mantle rigidity μ_m, and the Andrade parameter α fitting the empirical values of $k_{2,\mathrm{monthly}}$, $k_{3,\mathrm{monthly}}$, $h_{2,\mathrm{monthly}}$, $Q_{2,\mathrm{monthly}}$, and $(k_2/Q_2)_{\mathrm{annual}}$, while the other Andrade parameter was set to $\zeta = 1$. We generated $\sim 30,000$ random samples until the model converged. Specifically, the convergence was tested against the autocorrelation time of each variable in the ensemble, the total length of all chains being required to exceed 100 times the longest autocorrelation time. Moreover, in order to filter out the influence of initial conditions, we neglected the first $\sim 3,000$ samples (our burn-in period was, therefore, 10 times the autocorrelation time).

The posterior probabilities of the fitted parameters are depicted in Figure 3, using the *Python* library *corner* (Foreman-Mackey, 2016). In line with a similar model by Nimmo et al. (2012), we find a relatively high lunar mantle viscosity of $\log \eta[\mathrm{Pa\ s}] = 22.99^{+0.89}_{-1.35}$ and rigidity of $\log \mu[\mathrm{Pa}] = 10.92 \pm 0.06$, the Andrade parameter α being as low as $0.06^{+0.04}_{-0.02}$.

Treating the Andrade parameter ζ as a free parameter in the Bayesian inversion has a negligible effect on the predicted values of α and μ_m. However, it essentially determines the fitted mantle viscosity. If the transient deformation prevails over the viscous creep ($\zeta \ll 1$), the response of the lunar mantle to tidal loading is almost elastic (with viscosity up to $\eta \approx 10^{27}$ Pa s). On the other hand, if the dissipation is preferentially due to viscous creep ($\zeta \gg 1$), the mantle viscosity allowed by the observational data has to be much lower, $\eta \approx 10^{21}$ Pa s. This latter case is equivalent to the assumption that the mantle is governed by the Maxwell rheology, followed by Harada et al. (2014, 2016); Matsumoto et al. (2015); Tan and Harada (2021), and Kronrod et al. (2022).

If we compare the resulting Andrade parameter $\alpha = 0.06^{+0.04}_{-0.02}$ with the typical values reported in the literature ($0.1 < \alpha < 0.4$; see, e.g., the overview by Castillo-Rogez et al., 2011; Efroimsky, 2012a, 2012b), we may notice that it is unusually small. This discrepancy between our prediction and the laboratory data already indicates that although it is, in principle, possible to fit the lunar tidal response with a simple model assuming Andrade rheology in the mantle, the required parameters of this model might not be realistic. A similar point has been made by Khan et al. (2014) and used as an argument in favour of their interior model containing basal partial melt. Following the same line of argumentation, we will now focus our study on the Sundberg-Cooper model.

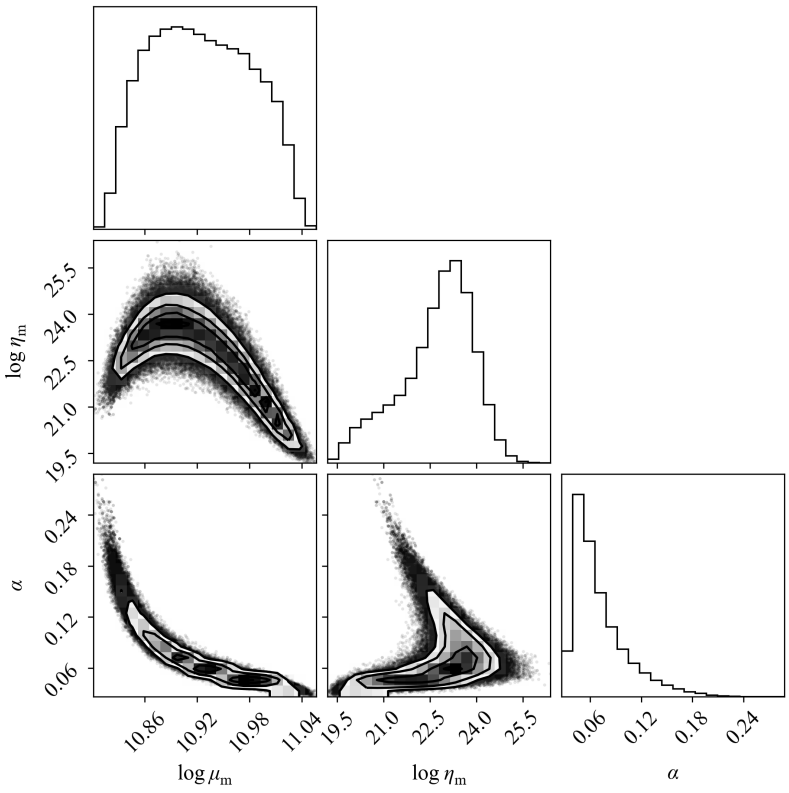

Figure 3. Posterior probabilities of the effective mantle rigidity μ_m, the mantle viscosity η_m, and the Andrade parameter α satisfying the full set of observational constraints (k_2, k_3, h_2, and Q at the monthly period; k_2/Q at the annual period). A model with a liquid core and a viscoelastic mantle governed by the Andrade rheology, assuming $\zeta = 1$.

5.5 Lunar Mantle Governed by the Sundberg-Cooper Model

In the present Subsection, as well as in Subsection 5.6, we will specifically search for lunar interior models that exhibit a second dissipation peak in the spectra of k_2/Q_2 and Q_2^{-1}. Since the current error bars of the empirical Qs allow for both a decrease and increase of dissipation with frequency, and since our study focuses on the latter case, we consider a hypothetical situation in which the uncertainty in Q_2 is comparable with the present-day uncertainty in k_2. The standard deviations of Q_2 at the monthly frequency and k_2/Q_2 at the annual frequency are thus arbitrarily set to 1% of the mean value. As in the previous inversion with Andrade mantle, we again employ the MCMC approach and seek the parameters of the Sundberg-Cooper model (η_m, μ_m, Δ, and t_rel) fitting the empirical tidal parameters. Values of α and ζ are kept constant. For illustration purposes, we consider both 1) a two-layered interior structure consisting of a liquid core and a viscoelastic (Sudberg-Cooper) mantle and 2) a homogeneous lunar interior. As we shall see, the effect of the small lunar core ($R_\mathrm{c} = 330\,\mathrm{km}$) on the results is negligible.

In contrast with the previous inversion, and mainly due to the greater dimension of the explored parameter space, the model only succeeded to converge after generating $\sim 700,000$ random samples. The posterior distributions of the tidal quality factors typically presented two peaks: a higher one with $Q_{2,\mathrm{monthly}} > Q_{2,\mathrm{annual}}$ and a lower one with $Q_{2,\mathrm{monthly}} < Q_{2,\mathrm{annual}}$. Here, we only discuss the model parameters corresponding to the latter case.

Figure 4 illustrates the results of the inversion with Andrade parameters specifically set to $\alpha = 0.2$ and $\zeta = 1$. Similarly as before, to filter-out the influence of initial conditions, we neglected the first $70,000$ samples. Then, 16% of the remaining, analysed samples fulfilled the condition of quality factor decreasing with frequency. The mean value of the predicted mantle viscosity lies close to $3.5{\times}10^{22}\,\mathrm{Pa\,s}$ and the predicted unrelaxed rigidity is around $60 - 120\,\mathrm{GPa}$. In particular, for the nominal case with $\alpha = 0.2$ and $\zeta = 1$ and for the arbitrarily chosen small standard deviation of empirical Q and k_2/Q, the decadic logarithms of the predicted mantle viscosity and rigidity are $\log \eta_\mathrm{m}[\mathrm{Pa\,s}] = 22.55^{+0.15}_{-0.54}$ and $\log \mu_\mathrm{m}[\mathrm{Pa}] = 10.84^{+0.14}_{-0.02}$. Increasing α by 0.1 or ζ by the factor of 10 results in decreasing the mantle viscosity approximately by an order of magnitude (and the same trend pertains to the other direction, when decreasing α or ζ). On the other hand, the mantle rigidity, being dictated by the magnitude of k_2, seems relatively robust and its inverted value does not depend on α.

The parameters of the Debye peak are, in this story, the key to fitting the unexpected slope of the frequency-dependent tidal dissipation. Independently of the considered Andrade parameters, the relaxation timescale τ lies between 10^4 and $10^6\,\mathrm{s}$ ($\log \tau[\mathrm{s}] = 4.89^{+0.62}_{-0.72}$), while the relaxation strength falls into the interval between 0.03 and 1 ($\log \Delta = -1.17^{+0.84}_{-0.35}$). The exact values depend on the predicted viscosity and rigidity, which define the position of the first peak, corresponding to the attenuation in the overlying mantle. Such short relaxation timescales would indicate that the elastically accommodated GBS is much faster than diffusion creep. For comparison, Sundberg and Cooper (2010) mention a GBS relaxation timescale of 0.1 s as a reasonable value in their experiments, using a material with $\tau_\mathrm{M} \sim 10 - 100\,\mathrm{s}$. Our τ_M in this specific case is in the order of $10^{10} - 10^{13}\,\mathrm{s}$; hence, the ratio of the two time scales for $\alpha = 0.2$ and $\zeta = 1$ reaches $t_\mathrm{rel} = 10^{-7} - 10^{-6}$. A more detailed discussion of this result will be provided in Subsection 6.1.

5.6 Comparison of a Sundberg-Cooper Moon with an Andrade Moon Having a Weak Basal Layer

As was recently shown by Gevorgyan (2021), the tidal response of a homogeneous Sundberg-Cooper planet mimics the response of a body consisting of two Andrade layers with different relaxation times. This kind of aliasing may, in principle, be demonstrated by the Moon. Figure 5 depicts the imaginary part of the tidal Love number (equal to

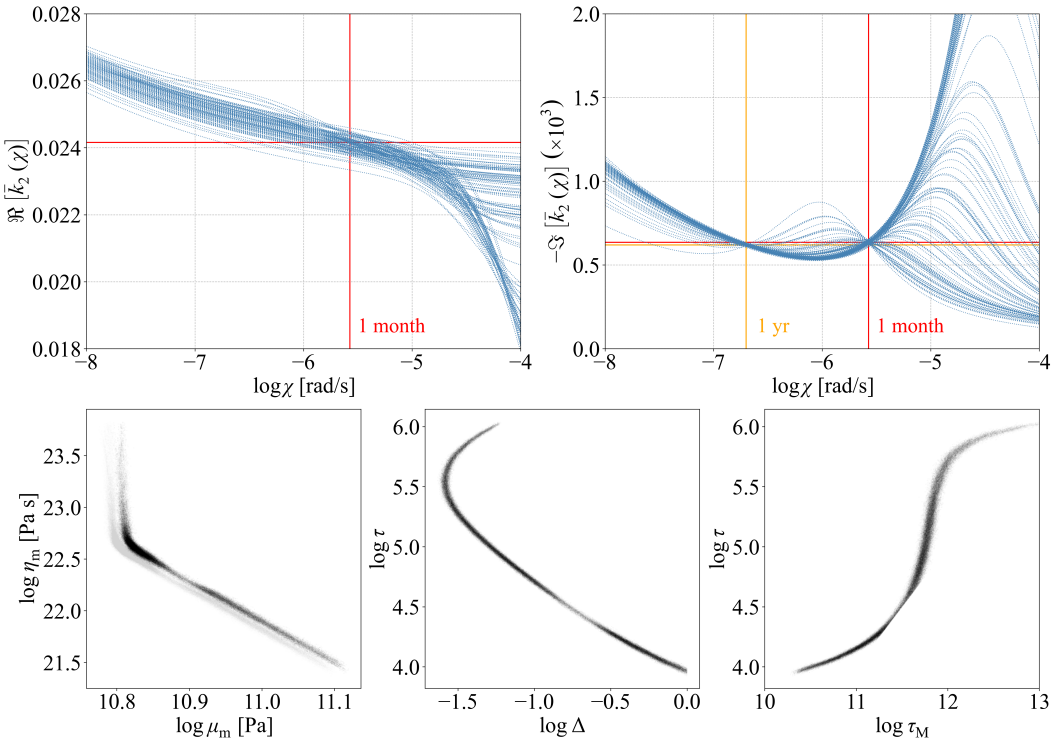

Figure 4. Best-fitting models and the corresponding model parameters for a melt-free Moon with a liquid core and a Sundberg-Cooper mantle. Upper row: the real (left) and negative imaginary (right) parts of the complex Love number $\bar{k}_2$, as functions of frequency. The red and yellow lines indicate the values provided by Williams and Boggs (2015). Lower row: model samples plotted in the parameter space, with the mantle rigidity μ_m depicted against viscosity η_m (left), the relaxation strength Δ depicted against the characteristic time τ of the elastically-accommodated GBS (centre), and the Maxwell time τ_M versus the characteristic time τ (right). The Andrade parameters are kept constant at $\alpha = 0.2$ and $\zeta = 1$. Gray dots in the lower left panel show the results obtained with a homogeneous model consisting only of a Sundberg-Cooper mantle, while black dots represent the default two-layered model.

k_2/Q_2) and the inverse quality factor $1/Q_2$ as functions of frequency, for a homogeneous Sundberg-Cooper moon and for a differentiated lunar interior with a rheologically weak layer at the base of the mantle. In the second case, the basal layer is described by the Maxwell model and the overlying mantle by the Andrade model. Both cases follow the same frequency dependence, implying that the existence of a weak basal layer cannot be confirmed unequivocally by the tidal data. In a layered model containing a core, a Sundberg-Cooper mantle, and a Maxwell basal semi-molten layer, the tidal response would be characterised by three peaks (Figure 6).

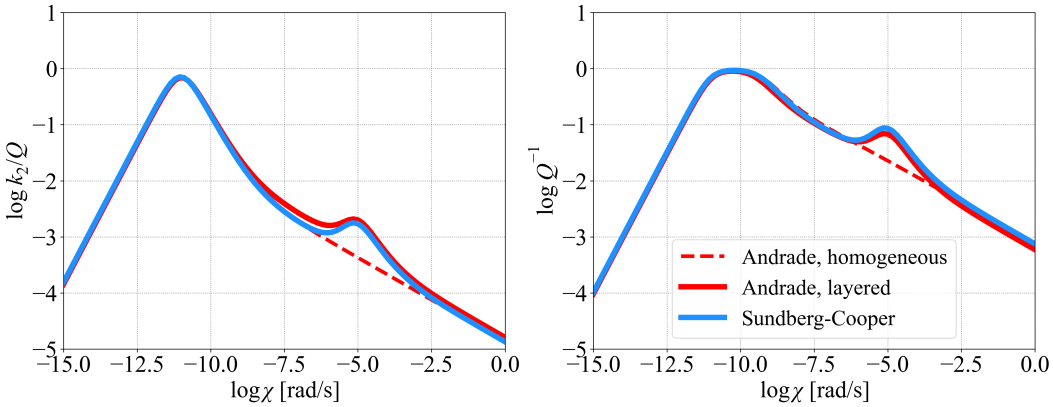

Figure 5. The negative imaginary part of the Love number (left) and inverse quality factor (right) for three model cases: a homogeneous Andrade model (dashed red line), a homogeneous Sundberg-Cooper model (blue line), and a three-layered model (solid red line) comprising a core, an Andrade mantle and a Maxwell semi-molten layer at the base of the mantle.

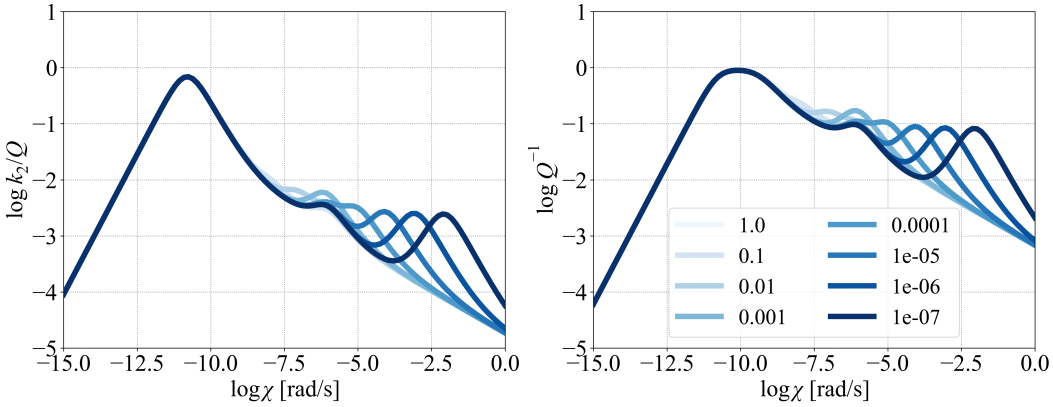

Figure 6. The negative imaginary part of the Love number (left) and inverse quality factor (right) of a three-layered lunar model comprising a core, a Sundberg-Cooper mantle, and a Maxwell semi-molten basal layer. Different shades of blue correspond to different ratios between the timescale τ and the Maxwell time τ_{M}. For illustrative purposes, the semi-molten basal layer is made unrealistically thick (500 km).

For comparison with other models presented in the literature, we also seeked for the parameters of a three-layered lunar model comprising a liquid core, an Andrade mantle, and a Maxwell basal low-viscosity layer that would fit the empirical constraints. As

in the previous Subsection, in order to reduce the number of unknowns, the parameters α and ζ of the Andrade model were kept constant. We also prescribed the same constant core radius of 330 km. The remaining quantities were treated as free parameters: we thus varied the rigidity and viscosity of the mantle and of the basal layer, and the outer radius of the basal layer. Due to the higher dimensionality of the parameter space, the inverse problem took longer to converge; therefore, we generated $10,000,000$ random samples satisfying all constraints from Table 2. Since the longest autocorrelation time in this case was $500,000$ steps, we discarded the first $5,000,000$ samples and then applied the condition $Q_{2,\mathrm{monthly}} < Q_{2,\mathrm{annual}}$, being left with 11% of the generated samples.

As illustrated in Figure 7, and in line with the discussion above, the frequency dependencies of $\Re[\bar{k}_2]$ and $-\Im[\bar{k}_2]$ in the model with a low-viscosity basal layer closely resemble those of the previous one, in which we considered the Sundberg-Cooper model. Similarly to the earlier predictions of the basal layer's viscosity and thickness (e.g., Harada et al., 2014, 2016; Matsumoto et al., 2015), we find that the observed frequency dependence of lunar Q_2^{-1} can be explained by the viscosity η_{LVZ} in the range from $\sim 10^{15}$ to $\sim 3{\times}10^{16}$ Pa s and the thickness D_{LVZ} in the range from 70 km to the maximum value considered in our model (370 km). The parameter dependencies of all model samples are plotted on Figure 8. For the nominal case with $\alpha = 0.2$ and $\zeta = 1$, and considering the condition on Q mentioned in the above paragraph, we obtain the following rigidity and viscosity of the overlying mantle and of the LVZ: $\log \eta_{\mathrm{m}}[\mathrm{Pa\ s}] = 22.79^{+0.19}_{-0.06}$, $\mu_{\mathrm{m}}[\mathrm{Pa}] = 10.89{\pm}0.03$, $\eta_{\mathrm{LVZ}}[\mathrm{Pa\ s}] = 15.20^{+0.53}_{-0.21}$, $\mu_{\mathrm{LVZ}}[\mathrm{Pa}] = 10.23^{+0.37}_{-0.34}$. The corresponding outer radius of the LVZ is $R_{\mathrm{LVZ}}[\mathrm{km}] = 599.39^{+65.83}_{-84.46}$.

Similarly to the "melt-free" case with the Sundberg-Cooper model, increasing α to 0.3 results in an order-of-magnitude decrease in the fitted mantle viscosity. Decreasing α to 0.1 leads to a mantle viscosity two orders of magnitude greater. On the other hand, the predicted properties of the semi-molten layer remain almost the same.

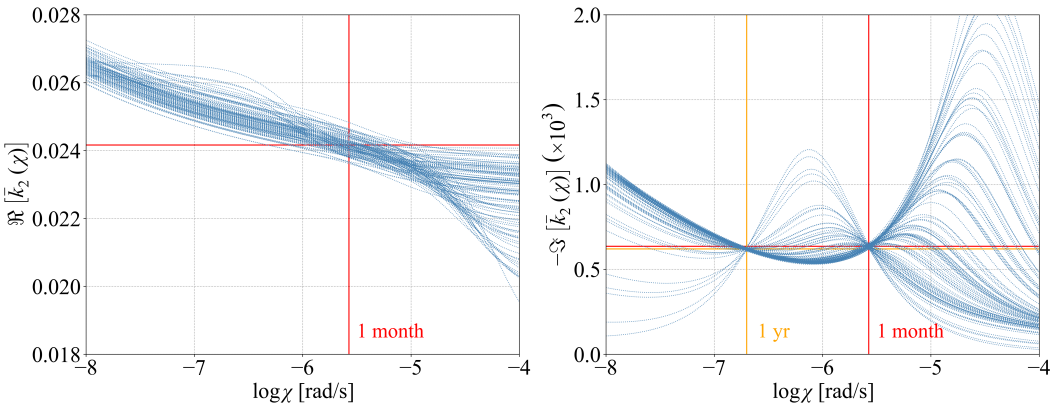

Figure 7. Overview of best-fitting models for the case with a basal low-viscosity zone. The red and yellow lines indicate the values provided by Williams and Boggs (2015). As in the previous inversion, the Andrade parameters are kept constant at $\alpha = 0.2$ and $\zeta = 1$, and the core size is fixed to 330 km.

6 Discussion

In the previous section, we have compared the frequency dependence of lunar Q within the widely accepted lunar interior model containing a highly dissipative layer at the base of the mantle (e.g., Nakamura et al., 1973; Williams et al., 2001; Harada et al., 2014) and within an alternative model taking into account the time relaxation of the elas-

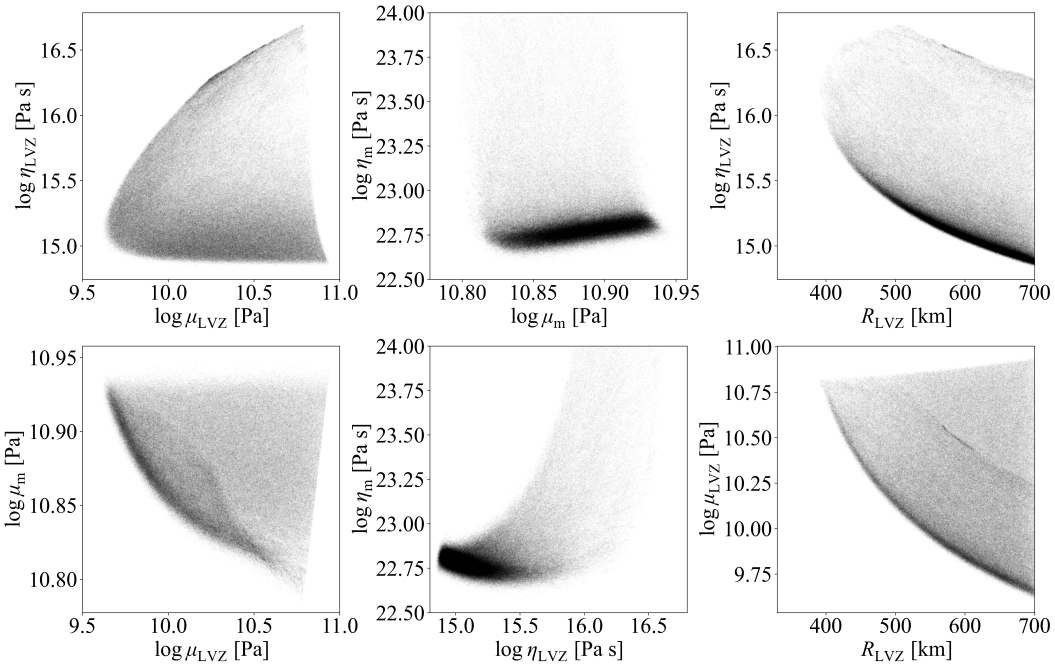

Figure 8. Model samples corresponding to Figure 7, plotted in the parameter space. The intensity indicates the sample count. Upper row: the rigidity vs. viscosity of the LVZ (left), the rigidity vs. viscosity of the mantle (centre), and the outer radius vs. viscosity of the LVZ (right). Lower row: the rigidity of the LVZ vs. rigidity of the mantle (left), the viscosity of the LVZ vs. viscosity of the mantle (centre), and the outer radius vs. rigidity of the LVZ (right).

tic compliance $J_{\rm e}$. On the following lines, we discuss the implications of each of the considered models for the lunar interior properties. Keep in mind that the inversions performed in our study explicitly assumed that the value of Q at the monthly frequency and k_2/Q at the annual frequency are known with a high precision. This is not the case in reality. However, as we have seen in Subsection 5.4, a lunar mantle governed by the Andrade model without a basal dissipative layer can fit the data with the actual uncertainties only for unrealistically low values of parameter α.

6.1 Melt-free Lunar Interior

In the model cases considering a two-layered, "melt-free" lunar interior, where the negative slope of the frequency dependence of k_2/Q is explained by a secondary dissipation peak induced by elastically accommodated GBS, we found that the logarithm of the relaxation timescale, $\log \tau$, falls into the range of $[4, 6]$, corresponding to τ between 3 and 300 hours. In the reference case depicted in Figure 4, this would imply a ratio of the characteristic timescales for the elastic and diffusional accommodation $t_{\rm rel} = \tau/\tau_M$ to be of order from 10^{-7} to 10^{-6}. Are such ratios of the characteristic times observed in any natural materials?

According to Jackson et al. (2014), grain boundary sliding comprises three processes. The relative contribution of each of them to the energy dissipation in a sample depends on the temperature and loading frequency. The processes are: (i) elastically accommodated GBS with a characteristic time τ, at high frequencies/low temperatures; (ii) diffusionally assisted GBS described by the power-law frequency-dependence of the *seismic* quality factor, $Q \propto \chi^p$; and (iii) diffusionally accommodated GBS at timescales

greater than the Maxwell time τ_M, where the seismic Q is a linear function of frequency, $Q \propto \chi$. The value of t_{rel} thus determines the range of frequencies over which the diffusionally assisted sliding on spacial scales smaller than grain size occurs. Experimental data for fine-grained polycrystals indicate that $t_{rel} \ll 1$ (Morris & Jackson, 2009).

Jackson et al. (2014) presented results of laboratory experiments on fine-grained olivine subjected to torsional oscillations at high pressures ($P = 200\,\mathrm{MPa}$) and relatively low temperatures ($T < 900\,^\circ\mathrm{C}$), i.e., around the threshold between elastic response and elastically accommodated GBS. They found a GBS relaxation timescale of $\log \tau_R = 1.15 \pm 0.07\,\mathrm{s}$, where the subscript "$R$" now stands for "reference". Considering the reference temperature $T_R = 900\,^\circ\mathrm{C}$, reference pressure $P_R = 200\,\mathrm{MPa}$, reference grain size $d_R = 10\,\mu\mathrm{m}$, activation volume $V^* = 10\,\mathrm{cm}^3\,\mathrm{mol}^{-1}$, and activation energy $E^* = 259\,\mathrm{kJ\,mol}^{-1}$, as given by Jackson et al. (2014), we can extrapolate τ to the conditions of the lunar mantle with the Arrhenius law (Jackson et al., 2010):

$$\tau = \tau_R \left(\frac{d}{d_R}\right)^m \exp\left\{\frac{E^*}{R}\left(\frac{1}{T} - \frac{1}{T_R}\right)\right\} \exp\left\{\frac{V^*}{R}\left(\frac{P}{T} - \frac{P_R}{T_R}\right)\right\} . \tag{46}$$

In addition to the parameters introduced earlier, d is the grain size and m characterises the grain-size dependence of the process in question. We adopt the value $m = 1.31$, found by Jackson et al. (2010) for anelastic processes. Figure 9 illustrates the extrapolation of τ_R of Jackson et al. (2014) to lunar interior conditions, considering our melt-free model and two depth-independent grain sizes. Over the colour-coded maps, we also plot the steady-state heat conduction profiles of Nimmo et al. (2012). We note that the conduction profiles were only chosen for illustration purposes: the discussion of the thermal regime (conductive vs. convective) in the lunar mantle is beyond the scope of this paper.

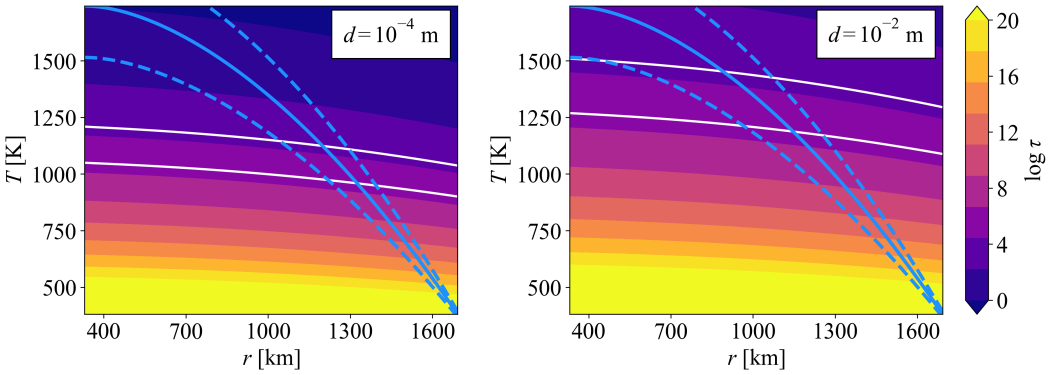

Figure 9. Relaxation time τ (colour-coded) of elastically accommodated GBS, as given by Jackson et al. (2014) and extrapolated to lunar interior conditions using the Arrhenian equation (46). White lines demarcate the relaxation times resulting from our inversion. Blue lines indicate analytically-calculated conduction profiles proposed by Nimmo et al. (2012) for three different mantle heat productions (8, 9.5, and 11 nW m^{-3}), crustal heat production of 160 nW m^{-3} crustal thickness of 45 km, and no heat exchange between core and mantle. Other parameters, such as the core size, core density, and mantle density, are adjusted to our melt-free model. Grain sizes are given in the upper right corner of each plot.

The laboratory measurements of Jackson et al. (2014) were performed on a single sample of fine-grained polycrystalline olivine under constant pressure P_R and the Arrhenian extrapolation of τ was only tested for temperature dependence. Nevertheless, if we

accept the assumption that these results are applicable to the Moon, Figure 9 and the fitted relaxation time from Figure 4 ($\log\tau \in [4,6]$) can help us to identify the minimum depth in which elastically accomodated GBS contributes to the tidal dissipation. For the smaller grain size ($d = 0.1\,\mathrm{mm}$) and the reference profile of Nimmo et al. (2012) (solid line, mantle heat production of $9.5\,\mathrm{nW\ m^{-3}}$), we predict the minimum depth of 400–500 km. For the larger grain size ($d = 1\,\mathrm{cm}$), the minimum depth is 600–800 km. A conductive profile corresponding to lower heat production than illustrated here would push the minimum depth to even greater values. The occurrence of elastically accommodated GBS in shallower depths would give rise to a relaxation peak (or to an onset of a relaxation band) at lower loading frequencies, which would not fit the observed annual and monthly tidal Q. Although the MCMC inversion from the previous section was performed for a model with a homogeneous mantle, i.e., assuming the occurrence of elastically-accommodated GBS at all depths from the surface down to the core, we also checked that a model described by the Andrade rheology above the derived depths and by the Sundberg-Cooper model below the derived depths would fit the considered observables under the condition that $\log\tau \gtrsim$. For shorter τ, the estimated minimum depth of applicability of the Sundberg-Cooper model would not match the Love numbers at monthly frequency.

Besides the timescale τ, we have derived the relaxation strength of the hypothetical secondary peak: $\log\Delta \in [-1.5, 0]$, or $\Delta \in [0.03, 1]$. Parameter Δ controls the height of the secondary dissipation peak in the Sundberg-Cooper model. Figure 10 shows the dependence of this Q^{-1} on the relaxation strength for all our models from Figure 4. Are these values consistent with theoretical prediction and laboratory data?

Sundberg and Cooper (2010) reported relaxation strengths of polycrystalline olivine between 0.23 and 1.91, as found in different sources and under different assumptions on the grain shapes (Kê, 1947; Raj & Ashby, 1971; Ghahremani, 1980). Their own mechanical tests on peridotite (olivine-orthopyroxene) at temperatures between 1200 and 1300 °C were best fitted with $\Delta = 0.43$ and the corresponding dissipation associated with elastically-accommodated GBS in their sample was $Q^{-1} = 0.25{-}0.3$. On the other hand, Jackson et al. (2014), who performed torsion oscillation experiments on olivine, found a relatively low dissipation peak with $Q^{-1} \leq 0.02$. Low secondary dissipation peaks with $Q^{-1} \sim 10^{-2}$ were also predicted theoretically by Lee and Morris (2010) for a grain boundary slope of 30°, while smaller slopes seem to allow Q^{-1} exceeding 1, especially when the individual grains are of comparable sizes and the grain boundary viscosity does not vary too much. Accordingly, Lee et al. (2011) note that Q^{-1} in the secondary peak depends strongly on the slope of the grain boundaries.

Following this brief discussion of dissipation arising due to elastically accommodated GBS, we can conclude that the relaxation strength Δ (or Q^{-1} in the secondary dissipation peak) is not well constrained and the values found in literature permit any of the Δs predicted in our Subsection 5.5.

6.2 Highly Dissipative Basal Layer

A highly dissipative layer located at any depth could also produce the desired secondary peak needed to explain the anomalous Q dependence. (Note, however, that a presence of a highly dissipative layer at a shallow depth may lead to changes in the body's response to tides and might be incompatible with the measured values of the Love numbers.) Petrological considerations combined with an indication of a basal low-velocity zone point to the presence of this anomalous layer in the deep interior. Therefore, as an alternative to the "melt-free" model, we tested the popular hypothesis of a putative highly dissipative layer at the base of the lunar mantle.

The derived rheological properties of the mantle and of the basal layer as well as the layer's thickness are poorly constrained and can be strongly biased. Firstly, the outer radius R_{LVZ} of the basal layer is correlated with the value of the mantle rigidity μ_{m}; the thicker the basal layer, the larger mantle rigidity can be expected to satisfy the model

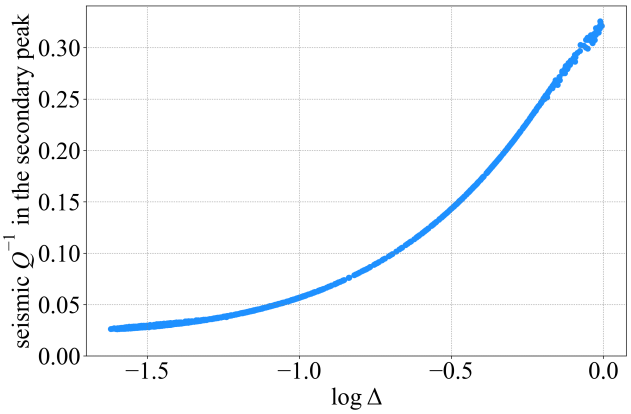

Figure 10. Seismic Q^{-1} of the mantle at the frequency of the secondary peak, plotted as a function of the relaxation strength Δ for models from Figure 4.

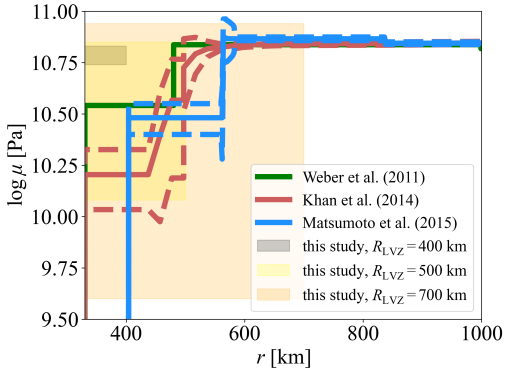

Figure 11. Shear modulus prediction compared to seismic measurements. Shear modulus μ_{LVZ} for R_{LVZ} = 400, 500 and 700 km (gray, yellow and orange areas). Shear modulus derived from seismic velocities and densities: green (Weber et al., 2011), red (Khan et al., 2014) and blue (Matsumoto et al., 2015), dashed lines: errors.

constraints. The mantle viscosity η_{m} depends on the empirical Andrade parameters, and an increase of α by 0.1 leads to a reduction of the fitted mantle viscosity approximately by one order of magnitude. On the other hand, the viscosity of the basal layer remains independent of the empirical Andrade parameters. The predicted contrast in viscosity between the two layers thus decreases with increasing α and/or ζ. Secondly, the range of acceptable basal rigidities μ_{LVZ} widens with the basal layer thickness (Figure 11). We do not find an acceptable solution for $R_{\mathrm{LVZ}} \lesssim 400\,\mathrm{km}$ due to our a priori requirement on the relationship between the mantle and basal layer's rigidities ($\mu_{\mathrm{LVZ}} \leq \mu_{\mathrm{m}}$). The range of acceptable μ_{LVZ} values increases with the basal layer radius up to one and a half order of magnitude for the maximum $R_{\mathrm{LVZ}} = 700\,\mathrm{km}$ considered here. Interestingly, the predicted rigidities of a basal layer with thickness $\sim 170\,\mathrm{km}$ ($R_{\mathrm{LVZ}} \approx 500\,\mathrm{km}$) corresponds well with the seismic observations. Lastly, the basal viscosity is correlated with the basal layer thickness: the viscosity η_{LVZ} decreases from $3{\cdot}10^{16}\,\mathrm{Pa\,s}$ for a thin weak layer ($R_{\mathrm{LVZ}} = 400\,\mathrm{km}$) to $< 10^{15}\,\mathrm{Pa\,s}$ for the greatest considered thickness ($R_{\mathrm{LVZ}} = 700\,\mathrm{km}$). The basal layer viscosity is, therefore, always considerably lower than the mantle viscosity. However, this is not surprising, as the low viscosity of this layer is essential to predict the anomalous frequency dependence of the tidal quality factor, when the rest of the high-viscosity mantle is set to obey the Andrade law.

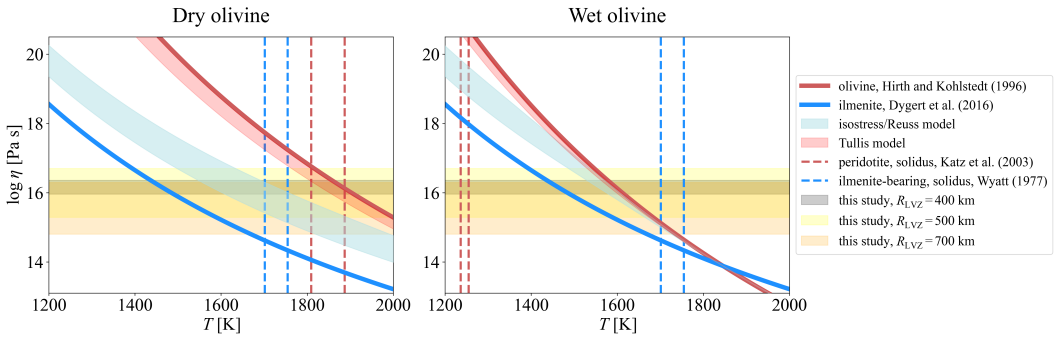

Figure 12. Basal viscosity prediction compared to rheological properties. Predicted ranges of viscosities η_{LVZ} for $R_{\mathrm{LVZ}} = 400$, 500 and 700 km are indicated by gray, yellow, and orange areas, respectively. Over the predicted ranges is plotted the temperature dependence of viscosity of ilmenite (blue, Dygert et al., 2016), dry olivine (red, Hirth & Kohlstedt, 1996), and ilmenite-olivine aggregate ($2 - 16\,\%$), the latter corresponding either to isostress (blue area, harmonic mean, suggested for high strain) or Tullis (red area, geometric mean, suggested for low strain) models. Errors of experimentally determined viscosities not included; ilmenite error factor is ~ 5. Vertical lines delimit solidus temperatures for peridotite (Katz et al., 2003) and ilmenite-bearing material (Wyatt, 1977) at radii 330 km and 700 km. Left panel: temperature dependence for $\sigma_D = 1\,\mathrm{MPa}$, dry olivine. Right panel: temperature dependence for $\sigma_D = 1\,\mathrm{MPa}$, wet olivine.

Rigidity and viscosity magnitudes, and their contrast between the mantle and the basal layer values, can be indicative of the variations in the composition, in the presence of melt, and in temperature. A stable partially molten zone in the lunar interior would pose strong constraints on the composition (Khan et al., 2014). Given the absence of geologically recent volcanic activity, any melt residing in the deep lunar interior would have to be neutrally or negatively buoyant. Using an experimental approach on the synthetic equivalent of Moon samples, van Kan Parker et al. (2012) concluded that the condition on the buoyancy below 1000 km is satisfied if high content of titanium dioxide is present in the melt. We can expect the presence of a partially molten layer at any depth below this neutral buoyancy level.

Moreover, evolutionary models suggest that high-density ilmenite bearing cumulates enriched with TiO_2 and FeO are created towards the end of the shallow lunar magma ocean crystallisation, resulting in near-surface gravitational anomalies. This instability, combined with the low viscosity of those cumulates, might have eventually facilitated the mantle overturn, creating an ilmenite-rich layer at the base of the mantle (e.g., Zhang et al., 2013; Zhao et al., 2019; Li et al., 2019). Recently, Kraettli et al. (2022) suggested an alternative compositional model: a ~ 70 km thick layer of garnetite could have been created at the base of the mantle if two independently evolving melt reservoirs were present. The resulting high-density garnet, olivine, and FeTi-oxide assemblage is gravitationally stable and can contain a neutrally or negatively buoyant Fe-rich melt. The scenario of Kraettli et al. (2022) can also be accompanied by the mantle overturn, as suggested for the ilmenite-rich layer created at shallow depths.

Rheologically weak ilmenite combined with appropriate lower-mantle temperature can help to explain the low basal viscosity (Figure 12). If the lower mantle were only made of dry olivine, the predicted viscosity would require temperature $\gtrsim 1800$ K, whereas for wet olivine, the temperature range between ~ 1500 and ~ 1800 K would be sufficient. Creep experiments (Dygert et al., 2016) conclude that the viscosity of ilmenite is more than three orders of magnitude lower than dry olivine. Consequently, a lower-mantle temperature ($1400 - 1700$ K) might be acceptable to explain the predicted viscosities for pure ilmenite. The properties of ilmenite-olivine aggregates introduce yet another complexity. The viscosity of aggregates is suggested to depend on the value of the strain: it follows the Tullis model for low strain, whereas it tends to follow the lower bound on Figure 12 (isostress model) for large strain (see, e.g., Dygert et al., 2016, for a deeper discussion). The acceptable temperature range for olivine-ilmenite aggregate is close to the values for the pure olivine in the case of the Tullis model. The prediction for the isostress model (minimum bound, Reuss model) is consistent with temperature values between $1500-1800$ K. Another obstacle in interpretation originates in the stress-sensitivity of the relevant creep. The viscosity can decrease by ~ 2.5 orders of magnitude while decreasing the differential stress by one order of magnitude. In terms of acceptable thermal state, the temperature consistent with our prediction would decrease roughly by ~ 100 K considering two-fold higher differential stress and increase by the same value for two-fold lower stress, respectively.

Consequently, we find acceptable solutions both below and above the solidus. Our three-layered model thus cannot exclude or confirm a possible partial melt presence. An alternative explanation for the viscosity reduction can be the presence of water (see also Karato, 2013, for a deeper dicussion), which would also reduce the solidus temperature and facilitate partial melting. Both the enrichment in ilmenite and elevated water content can lead to the desired value of viscosity at lower temperatures compared to the dry and/or ilmenite-free models (Figure 12).

Focusing now on the elastic properties, we note that the rigidities of olivine (e.g. Mao et al., 2015), ilmenite (Jacobs et al., 2022), and garnetite (Kraettli et al., 2022) are comparable. The temperature has only a limited impact on their value (-0.01 GPa/K for olivine and ilmenite). Also, dependence on the water content (olivine-brucite) is only moderate (-1.3 GPa/wt%; Jacobsen et al., 2008). The magnitude of rigidity is, therefore, rather insensitive to possible constituents, temperature and water content. The upper bound of basal layer's rigidity predicted here (~ 60 GPa for $R_{\mathrm{LVZ}} = 400$ km, ~ 70 GPa for $R_{\mathrm{LVZ}} = 500$ km and ~ 85 GPa for $R_{\mathrm{LVZ}} = 700$ km) fits the elastic properties of all considered minerals—ilmenite, olivine, and garnet. However, the lower bound values (for $R_{\mathrm{LVZ}} > 500$ km) are difficult to explain by the changes in composition, high temperature, and/or water content.

The magnitude of rigidity (Figure 13) is, nevertheless, sensitive to the presence of melt around or above the disintegration point (characterised by the critical porosity ϕ_{c}), which describes the transition from the solid to liquid behaviour and its typical values

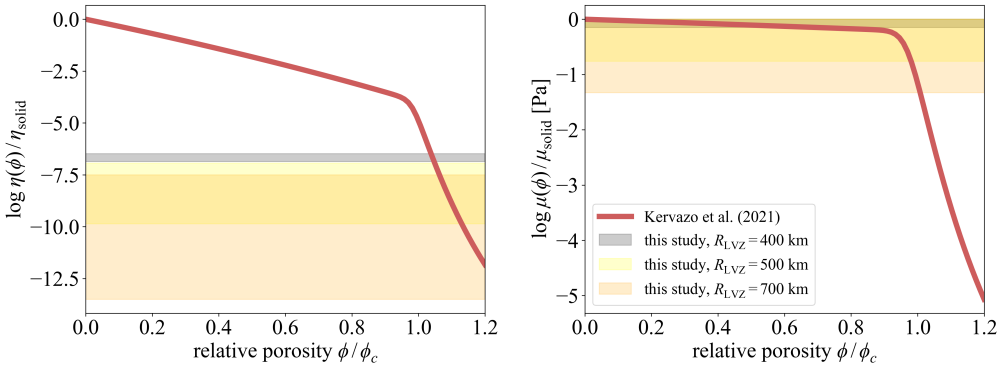

Figure 13. Impact of melt on the viscosity and rigidity contrast. The viscosity and rigidity contrast expressed as a function of the ϕ/ϕ_c (ϕ denotes the porosity and ϕ_c the critical porosity and parameterised using Kervazo et al. (2021); η_{solid} and μ_{solid} represents values with no melt present at the solidus temperature; no change in composition is considered. The shaded areas depict the predicted contrasts.

lie between 25−40%. Similarly, the viscosity value is very sensitive to the presence of melt for porosity higher than ϕ_c. For low porosities, it follows an exponential (Arrhenian) dependence. Figure 13 suggest that the predicted rheological contrasts in the nominal case are consistent with $\phi \lesssim 1.1\phi_c$ for shear modulus contrast and with $\phi > 1.1\phi_c$ for the viscosity contrast. This apparent inconsistency may be accounted for by the presence of melt accompanied by the changes in composition of the basal layer and by the susceptibility of viscosity to these changes. Consequently, the knowledge of the contrasts in both rheological parameters (rigidity and viscosity) could help tackle the trade-offs between porosity content and composition/temperature. Nevertheless, we must emphasise that the viscosity contrast predicted by our models is sensitive to the Andrade parameters of the mantle, leading to another uncertainty.

The presence of a partially molten material would pose a strong constraint on the temperature and possible mode of the heat transfer in the lower mantle of the Moon, allowing only models that reach the temperature between the solidus and liquidus (Figure 14). The traditional advective models predict stagnant-lid convection with a relatively thick lid at present (e.g. Zhang et al., 2013). Below the stagnant lid, the temperature follows the adiabatic or, for large internal heating, sub-adiabatic gradient. We estimate the temperature increase across the entire mantle due to the adiabatic gradient to be bounded by 100 K. Within those traditional models, it is plausible to reach solidus only in the lowermost thermal-compositional boundary layer. In the case of conductive models (e.g. Nimmo et al., 2012), the temperature gradient is steeper than the solidus gradient and the solidus temperature can be reached in the entire basal layer, given appropriate internal heating (as demonstrated in Figure 14). Interestingly, the lunar selenotherm determined by the inversions of lunar geophysical data combined with phase-equilibrium computations (Khan et al., 2014) lies between the conductive and adiabatic gradients.

In the future, distinct sensitivity of rigidity, viscosity, and other transport properties to temperature, melt fraction, and composition may provide a way to separate the interior thermal and composition structure. At present, inversion errors and the uncertainties on material properties cannot confirm or rule out the existence of a partially molten basal layer. It therefore remains a valid hypothesis.

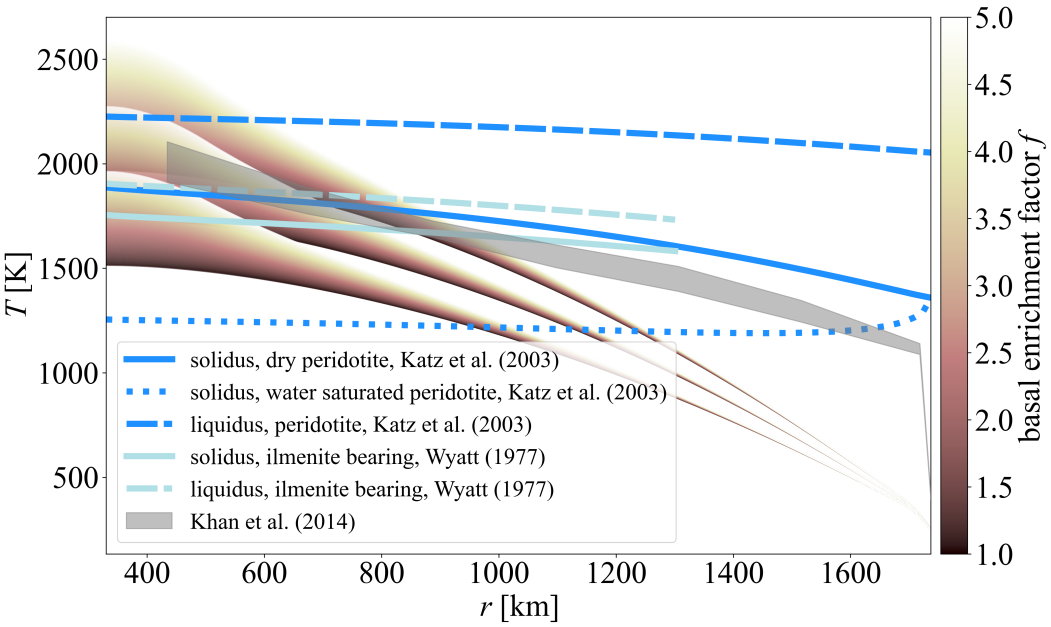

Figure 14. Comparison of temperature profiles. Colour scale: conductive profile, calculated with the matrix propagator method; parameters as in Figure 9. Individual branches correspond to average heating 8, 9.5 and 11 $\mathrm{nW/m^2}$ in the mantle. The coefficient f denotes the enrichment in the radiogenic elements of the basal layer ($R_{\mathrm{LVZ}} = 500\,\mathrm{km}$) compared to the rest of the mantle. Gray area is the temperature profile adapted from Khan et al. (2014); darker blue lines: peridotite solidus (solid), water-saturated solidus (dotted), and liquidus (dashed) according to Katz et al. (2003); light blue lines: clinopyroxene+ilmenite solidus (solid) and liquidus (dashed) according to Wyatt (1977).

6.3 Other Sources of Information

The two models discussed here — one with a highly dissipative basal layer and the other with elastically-accommodated GBS in the mantle — cannot be distinguished from each other by the available selenodetic measurements. To answer the question stated in the title of our paper, one would need to resort to other types of empirical data. Among all geophysical methods devised for the exploration of planetary interiors, seismology is of foremost importance. Therefore, a question that cannot be solved by the interpretation of lunar tidal response might be answered by comparing the arrival times and the phases detected at individual seismic stations.

As we mentioned in Introduction, the Moon demonstrates a nearside-farside seismic asymmetry. Judging by the currently available seismic data collected on the near side, the deep interior of the far side is virtually aseismic or, alternatively, the seismic waves emanating from it are strongly attenuated or deflected. The existence of an aseismic area on the farside might not be entirely inconceivable. First, as pointed out by Nakamura (2005), there are large zones with no located nests of deep moonquakes even on the nearside; and, in fact, most of the known deep seismic nests are part of an extended belt reaching from the south-west to the north-east of the lunar face. Second, there exists a pronounced dichotomy between the near side and far side of the Moon in terms of the crustal thickness, gravity field, and surface composition, which might point to a deeper, internal dichotomy as predicted by some evolutionary models (e.g., Laneuville et al., 2013; Zhu et al., 2019; Jones et al., 2022).

An obvious way to illuminate the lack of deep farside moonquakes detected by the Apollo seismic stations would be to place seismometers on the far side of the Moon. They would observe the far side activity, and record the known repeating nearside moonquakes or events determined from impact flash observations. The Farside Seismic Suite (FSS) mission, recently selected for flight as part of the NASA PRISM program and planned for launch in 2024 or 2025, might provide such a measurement by delivering two seismometers to Schrödinger Crater (Panning et al., 2021). While this crater is far from the antipodes (in fact, close to the South pole), a seismometer residing in it should still be able to detect events from the far side, thereby addressing the hemispheric asymmetry in the Apollo observations. However, resolving polarisation of arrivals may be challenging for many moonquakes, meaning that many events will only have distance estimated, but not azimuth. (We are grateful to Mark P. Panning for an enlightening consultation on this topic.)

A better site for this science objective would be the far side Korolev crater residing by the equator, about 23 degrees from the antipodes. It is now considered as one of the possible landing sites for the Lunar Geophysical Network (LGN) mission proposed to arrive on the Moon in 2030 and to deploy packages at four locations to enable geophysical measurements for 6 - 10 years (Fuqua Haviland et al., 2022).

Still, having a station or even an array of seismic stations at or near the antipodes would be ideal. Observed by such a station or stations, all events at distances less than 90 degrees from the antipodes could be confidently assigned to the far side. So we would recommend the near-antipodes zone as a high-priority landing site for some future mission, a perfect area to monitor the seismic activity on the far side and, especially, to observe if and how seismic waves proliferate through the base of the mantle.

In addition to seismic measurements, and similarly to what is predicted for Jupiter's volcanic moon Io or for icy moons with subsurface oceans, the presence of a highly dissipative or a partially molten layer might be reflected in the tidal heating pattern on lunar surface (e.g., Segatz et al., 1988; Tobie et al., 2005). However, as illustrated in the upper row of Figure 15, the positioning of the layer at the base of the mantle results in a very small difference between the surface heating patterns corresponding to the two alternative models. Both models show maxima of the average surface tidal heat flux $\Phi_{\rm tide}$ on the lunar poles and minima on the "subterranean" ($\varphi = 0$) and antipodal ($\varphi = \pi$)

points. Moreover, the magnitude of Φ_{tide} is generally very small, about three orders of magnitude lower than the flux produced by radiogenic heating of lunar interior (e.g., Siegler & Smrekar, 2014). The detection of any differences between the surface heat flux of the two models would be extremely challenging, if not impossible.

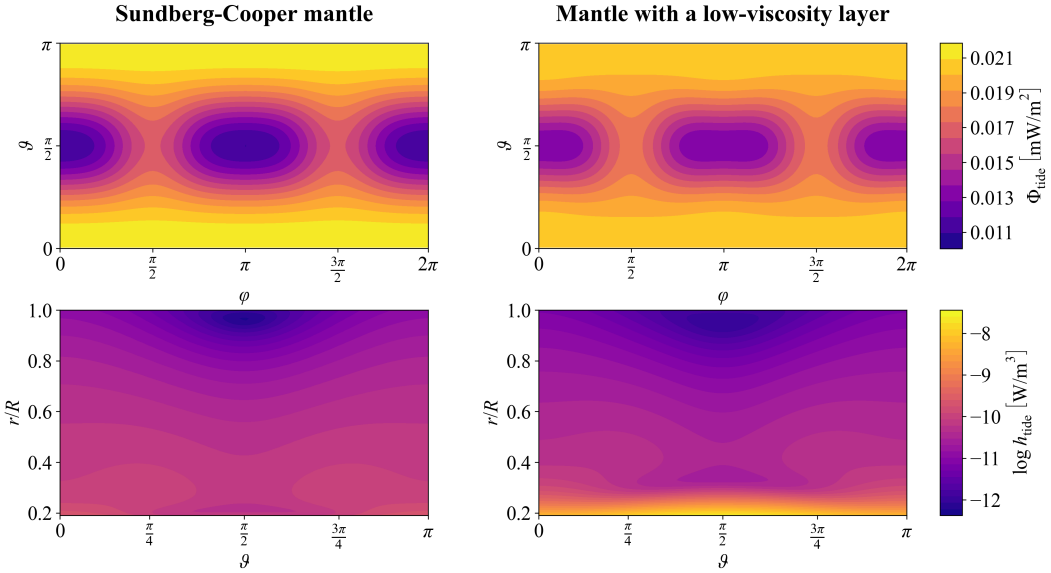

Figure 15. Average surface tidal heat flux (top) and volumetric tidal heating (bottom) for a specific realisation of each of the two models discussed in this work: the model considering elastically-accommodated GBS through the Sundberg-Cooper rheological model (left) and the model with a basal low-viscosity zone (right). In particular, the volumetric tidal heating is plotted as a function of relative radius r/R and colatitude ϑ with longitude φ equal to 0.

The lower row of Figure 15 illustrates volumetric heat production due to tidal dissipation. As pointed out by Harada et al. (2014), the presence of a low-viscosity zone at the base of the mantle results in considerable local increase of tidal heating with respect to the rest of the mantle or to the model without the basal layer. While the tidal contribution to heat production in the high-viscosity parts of the mantle is around 10^{-11} W m^{-3}, the tidal heat production in the basal layer reaches $\sim 10^{-8}$ W m^{-3}. For comparison, the global average of mantle heat production by all sources (radiogenic and tidal) is estimated to be 6.3×10^{-9} W m^{-3} (Siegler & Smrekar, 2014). The predicted tidal dissipation in the basal layer can help to locally increase the temperature and exceed the solidus, especially if conductive heat transfer prevails in the lunar mantle. Combined with a high enrichment of the basal layer in heat producing elements, it may then contribute to maintaining the presence of melt.

Although virtually discarded in the beginning of this Subsection, let us nevertheless discuss possible insights provided by future high-precision tidal measurements. At present, the quality factor Q at tidal frequencies is obtained exclusively from fitting the lunar physical libration, empirically determined by LLR. However, increased precision of satellite tracking (Dirkx et al., 2019; Hu et al., 2022; Stark et al., 2022) might eventually enable the determination of lunar tidal phase lag from the gravity field. Having an independent determination of tidal Q, which is related to the phase lag, would serve as a verification of the method used for fitting the LLR time series.

Among the quantities that we used in the inversion was degree-3 potential Love number k_3. This parameter is currently only known with a large error bar but its refine-

ment would only help to discern between the two alternative models considered here if the elastically-accommodated GBS was contributing to the dissipation throughout the entire mantle (and not only in greater depths, as tentatively derived in Subsection 6.1). This is a consequence of a degree-dependent sensitivity of Love numbers to the interior structure. While degree-2 Love numbers and quality factors probe the lunar interior down to the core, higher-order quantities are only sensitive to shallower depths. The Love number k_3—or the quality factor Q_3—would thus not "see" the basal low-viscosity layer, but it might sense complex tidal response in the upper mantle. As a result, the detection of the unexpected frequency dependence of tidal dissipation even in Q_3 (accompanied by a relatively high $k_3 \sim 0.01$) would clearly point at a mechanism acting in shallow depths.

Interestingly, the two alternative models can be better distinguished from each other in case the secondary peak of tidal dissipation, resulting either from the existence of a weak basal layer or from the Sundberg-Cooper model, lies at frequencies close to $10^{-4}\,\mathrm{rad\,s^{-1}}$. Then, provided that the elastically-accommodated GBS is only active below distinct depths (400−600 km), one could see a difference in predicted h_2 of the two models. Independently on that depth, the models with secondary dissipation peak close to $10^{-4}\,\mathrm{rad\,s^{-1}}$ also differ in elastic Love number $k_{2,\mathrm{e}}$, which can be calculated for interior structures obtained from the inversion of seismic waves (as was done by Weber et al., 2011). Specifically, $k_{2,\mathrm{e}}$ in the melt-free model is then much lower that that of the model with a weak basal layer. The value reported by Weber et al. (2011), which is $k_{2,\mathrm{e}} = 0.0232$, is attained by both the alternative models for a secondary tidal dissipation peak lying at $\sim 10^{-5.5}\,\mathrm{rad\,s^{-1}}$. In that case, the models are already indistinguishable. Seismic Q in the melt-free part of the mantle (at 1 Hz) for the models mentioned in the previous sentence is around $800 - 1000$.

Finally, we would like to note that any increase in the precision of Q determination will greatly help in answering the question whether any specific source of additional dissipation, be it a weak basal layer or elastic accommodation of strain at grain boundaries, is necessary in the first place. Recall that in order to fit the two alternative models to the tidal data, we assumed that the uncertainty on Q is of the order of 1% the mean value. In reality, the empirical Q at the monthly and the annual frequencies present an uncertainty between 10 and 20%. Keeping the original uncertainties, we were still able to fit the tidal data with the standard Andrade model, although with an unrealistically small exponential factor.

7 Conclusions

Tidal effects strongly depend not only on the interior density, viscosity, and rigidity profiles of celestial bodies, but also on the implied deformation mechanisms, which are reflected in the rheological models adopted. In this work, we attempted to illustrate that the unexpected frequency dependence of the tidal Q measured by LLR (Williams & Boggs, 2015) can be explained by lunar interior models both with and without a partially molten basal layer, and that each of the considered models leads to a different set of constraints on the interior properties.

As a first guess, we fitted the lunar tidal parameters (k_2, k_3, h_2, Q at the monthly frequency and k_2/Q at the annual frequency) with a model consisting of a fluid core and a viscoelastic mantle governed by the Andrade rheology. Within that model, and setting $\zeta = 1$ (i.e., the time scales of viscoelastic and anelastic deformation were considered comparable) we found a mantle viscosity of $\log \eta_{\mathrm{m}}[\mathrm{Pa\,s}] = 22.99^{+0.89}_{-1.35}$, mantle rigidity of $\log \mu_{\mathrm{m}}[\mathrm{Pa}] = 10.92 \pm 0.06$, and the Andrade parameter α as low as $0.06^{+0.04}_{-0.02}$. The predicted value of α is generally lower than reported in the literature (0.1-0.4; e.g., Jackson et al., 2010; Castillo-Rogez et al., 2011; Efroimsky, 2012a, 2012b). This observation leads us to the conclusion that the tidal response of the Moon probably cannot be explained by the Andrade model alone and requires either a basal low-viscosity zone (in

line with the conclusion of Khan et al., 2014) or an additional dissipation mechanism in the mantle (similar to Nimmo et al., 2012).

Throughout Section 5, we have seen that the two alternative models expected to explain the anomalous frequency dependence of lunar Q (assumed to be known with an arbitrarily chosen high precision) cannot be distinguished from each other by the existing measurements of tidal deformation and dissipation alone. In the two-layered model consisting of a liquid core and a Sundberg-Cooper mantle, the fitting of tidal parameters requires the relaxation time τ associated with elastically-accommodated GBS to be in the range from 3 to 300 hours. The corresponding relaxation strength Δ is predicted to lie in the interval $[0.03, 1]$. For a nominal case with Andrade parameters $\alpha = 0.2$ and $\zeta = 1$, we further obtain a mantle viscosity of $\log \eta_\mathrm{m}[\mathrm{Pa\ s}] = 22.55^{+0.15}_{-0.54}$ and a mantle rigidity $\log \mu_\mathrm{m}[\mathrm{Pa}] = 10.84^{0.14}_{-0.02}$.

In the three-layered model containing a liquid core, a low-rigidity basal layer, and an Andrade mantle, the tidal parameters are consistent with a wide range of basal layer thicknesses D_LVZ and rigidities μ_LVZ. As a general rule, a thicker layer implies weaker constraints on its rigidity, allowing both melt-like and solid-like behaviour. The predicted values of μ_LVZ are consistent with elastic properties of all considered minerals (olivine, ilmenite, granite) and with a wide range of lower-mantle temperatures. In contrast to the rigidity, the viscosity η_LVZ of the basal layer is constrained relatively well and falls into the range from about 10^{15} to 3×10^{16} Pa s, with a preference for the lower values ($\log \eta_\mathrm{LVZ}[\mathrm{Pa\ s}] = 15.20^{+0.53}_{-0.21}$). This is also in accordance with the results of Efroimsky (2012a, 2012b); Harada et al. (2014, 2016); Matsumoto et al. (2015); Tan and Harada (2021), and Kronrod et al. (2022). Nevertheless, even the viscosity is not able to pose strong constraints on the lower-mantle temperature, owing to the large uncertainties both on tidal Q and on the rheological properties of lunar minerals. For the viscosity and rigidity of the overlying mantle in the nominal case, we get $\log \eta_\mathrm{m}[\mathrm{Pa\ s}] = 22.79^{+0.19}_{-0.06}$ and $\log \mu_\mathrm{m}[\mathrm{Pa}] = 10.88 \pm 0.03$.

The existence of a basal weak or possibly semi-molten layer in the mantles of terrestrial bodies has been recently also suggested for Mercury (Steinbrügge et al., 2021) and for Mars (Samuel et al., 2021). In the case of Mercury, a lower mantle viscosity as low as 10^{13} Pa s was proposed to match the latest measurements of the moment of inertia and of k_2; although this result was later critically reassessed by Goossens et al. (2022), who showed that more realistic values around 10^{18} Pa s might still explain the observations. In the case of Mars, the putative basal semi-molten layer was introduced by Samuel et al. (2021) to provide an alternative fit to seismic data which would not require the existence of a large core with unexpectedly high concentration of light elements (reported in Stähler et al., 2021). Lastly, large provinces of decreased shear seismic velocities also exist at the base of the Earth's mantle. These zones form a heterogeneous pattern in the deep terrestrial interior; however, according to numerical models, the formation of a continuous layer right above the core-mantle boundary is also possible for some values of model parameters (e.g., Dannberg et al., 2021). A new question thus arises: is a weak basal layer something common among terrestrial planet's mantles? Is it a natural and widely present outcome of magma ocean solidification and subsequent dynamical processes? Or is it merely a popular explanation of the data available?

Since the available tidal parameters were deemed insufficient to distinguish a weak basal layer above the lunar core from the manifestation of elastically accommodated GBS in the mantle, we conclude that an answer to the question stated in the title of our paper awaits future lunar seismic experiments (ideally with a uniform distribution of seismometers across the lunar surface) as well as a better understanding of elastic parameters of olivine-ilmenite assemblages near their melting point. Additionally, a tighter bound on the hypothetical basal layer parameters or on the strength and position of the secondary Debye peak in the alternative, Sundberg-Cooper model might be given by updated values of tidal Q at multiple frequencies or by an independent inference of inte-

rior dissipation from the tidal phase lag and frequency-dependent k_2, theoretically measurable by laser altimetry or orbital tracking data (Dirkx et al., 2019; Hu et al., 2022; Stark et al., 2022). A combination of all those sources of information will probably still not provide a bright picture of deep lunar interior; however, it will help us to refute at least some of the many possible interior models.

Open Research

The software developed for the calculation of tidal Love numbers and quality factors of multi-layered bodies, the Python interface for running the MCMC inversion, and the plotting tools used for the figures presented in this study will be made available at the GitHub repository of the corresponding author (`https://github.com/kanovami/Lunar_Q`) and preserved at [DOI to be added later during the peer review process] under the licence [to be added later during the peer review process].

Acknowledgments

The authors would like to thank James G. Williams and Mark P. Panning for extremely helpful conversations on various aspects of the lunar science. M.W. is grateful to Ana-Catalina Plesa and Martin Knapmeyer for discussions about the lunar interior and to Philipp A. Baumeister for introducing her to the Python libraries used in this work. She also gratefully acknowledges the financial support and endorsement from the DLR Management Board Young Research Group Leader Program and the Executive Board Member for Space Research and Technology. M.B. received funding from Czech Science Foundation grant no. GA22-20388S.

References

Bagheri, A., Efroimsky, M., Castillo-Rogez, J., Goossens, S., Plesa, A.-C., Rambaux, N., ... Giardini, D. (2022, August). Tidal insights into rocky and icy bodies: An introduction and overview. *Advances in Geophysics*, *63*, 231-320.

Biot, M. A. (1954). Theory of stress-strain relations in anisotropic viscoelasticity and relaxation phenomena. *Journal of Applied Physics*, *25*(11), 1385–1391.

Bolmont, E., Breton, S. N., Tobie, G., Dumoulin, C., Mathis, S., & Grasset, O. (2020, December). Solid tidal friction in multi-layer planets: Application to Earth, Venus, a Super Earth and the TRAPPIST-1 planets. Potential approximation of a multi-layer planet as a homogeneous body. *Astronomy & Astrophysics*, *644*, A165. doi: 10.1051/0004-6361/202038204

Boué, G., & Efroimsky, M. (2019). Tidal evolution of the keplerian elements. *Celestial Mechanics and Dynamical Astronomy*, *131*, 30. doi: 10.1007/s10569-019-9908-2

Castillo-Rogez, J. C., Efroimsky, M., & Lainey, V. (2011, September). The tidal history of Iapetus: Spin dynamics in the light of a refined dissipation model. *Journal of Geophysical Research (Planets)*, *116*(E9), E09008. doi: 10.1029/2010JE003664

Dannberg, J., Myhill, R., Gassmöller, R., & Cottaar, S. (2021, November). The morphology, evolution and seismic visibility of partial melt at the core-mantle boundary: implications for ULVZs. *Geophysical Journal International*, *227*(2), 1028-1059. doi: 10.1093/gji/ggab242

Darwin, G. H. (1879, January). On the Analytical Expressions Which Give the History of a Fluid Planet of Small Viscosity, Attended by a Single Satellite. *Proceedings of the Royal Society of London Series I*, *30*, 255-278.

Dirkx, D., Prochazka, I., Bauer, S., Visser, P., Noomen, R., Gurvits, L. I., & Vermeersen, B. (2019, November). Laser and radio tracking for planetary science missions—a comparison. *Journal of Geodesy*, *93*(11), 2405-2420. doi:

10.1007/s00190-018-1171-x

Dumoulin, C., Tobie, G., Verhoeven, O., Rosenblatt, P., & Rambaux, N. (2017, June). Tidal constraints on the interior of Venus. *Journal of Geophysical Research (Planets)*, *122*(6), 1338-1352. doi: 10.1002/2016JE005249

Dygert, N., Hirth, G., & Liang, Y. (2016). A flow law for ilmenite in dislocation creep: Implications for lunar cumulate mantle overturn. *Geophysical Research Letters*, *43*(2), 532-540. Retrieved from `https://agupubs.onlinelibrary.wiley.com/doi/abs/10.1002/2015GL066546` doi: https://doi.org/10.1002/2015GL066546

Efroimsky, M. (2012a, March). Bodily tides near spin-orbit resonances. *Celestial Mechanics and Dynamical Astronomy*, *112*(3), 283-330. doi: 10.1007/s10569-011-9397-4

Efroimsky, M. (2012b, February). Tidal Dissipation Compared to Seismic Dissipation: In Small Bodies, Earths, and Super-Earths. *The Astrophysical Journal*, *746*(2), 150. doi: 10.1088/0004-637X/746/2/150

Efroimsky, M. (2015, October). Tidal Evolution of Asteroidal Binaries. Ruled by Viscosity. Ignorant of Rigidity. *The Astronomical Journal*, *150*(4), 98. doi: 10.1088/0004-6256/150/4/98

Efroimsky, M., & Makarov, V. V. (2013). Tidal friction and tidal lagging. applicability limitations of a popular formula for the tidal torque. *The Astrophysical Journal*, *764*, 26. doi: 10.1088/0004-637X/764/1/26

Efroimsky, M., & Makarov, V. V. (2014, November). Tidal Dissipation in a Homogeneous Spherical Body. I. Methods. *The Astrophysical Journal*, *795*(1), 6. doi: 10.1088/0004-637X/795/1/6

Foreman-Mackey, D., Hogg, D. W., Lang, D., & Goodman, J. (2013, March). emcee: The MCMC Hammer. *Publications of the Astronomical Society of the Pacific*, *125*(925), 306. doi: 10.1086/670067

Foreman-Mackey, D. (2016, jun). corner.py: Scatterplot matrices in python. *The Journal of Open Source Software*, *1*(2), 24. Retrieved from `https://doi.org/10.21105/joss.00024` doi: 10.21105/joss.00024

Frohlich, C., & Nakamura, Y. (2009, April). The physical mechanisms of deep moonquakes and intermediate-depth earthquakes: How similar and how different? *Physics of the Earth and Planetary Interiors*, *173*(3-4), 365-374. doi: 10.1016/j.pepi.2009.02.004

Fuqua Haviland, H., Weber, R. C., Neal, C. R., Lognonné, P., Garcia, R. F., Schmerr, N., ... Bremner, P. M. (2022, February). The Lunar Geophysical Network Landing Sites Science Rationale. *The Planetary Science Journal*, *3*(2), 40. doi: 10.3847/PSJ/ac0f82

Garcia, R. F., Gagnepain-Beyneix, J., Chevrot, S., & Lognonné, P. (2011, September). Very preliminary reference Moon model. *Physics of the Earth and Planetary Interiors*, *188*(1), 96-113. doi: 10.1016/j.pepi.2011.06.015

Garcia, R. F., Khan, A., Drilleau, M., Margerin, L., Kawamura, T., Sun, D., ... Zhu, P. (2019, November). Lunar Seismology: An Update on Interior Structure Models. *Space Science Reviews*, *215*(8), 50. doi: 10.1007/s11214-019-0613-y

Gerstenkorn, H. (1967, January). The Earth as a Maxwell body. *Icarus*, *6*(1-3), 92-99. doi: 10.1016/0019-1035(67)90006-1

Gevorgyan, Y. (2021, June). Homogeneous model for the TRAPPIST-1e planet with an icy layer. *Astronomy & Astrophysics*, *650*, A141. doi: 10.1051/0004-6361/202140736

Ghahremani, F. (1980). Effect of grain boundary sliding on anelasticity of polycrystals. *International Journal of Solids and Structures*, *16*(9), 825-845. Retrieved from `https://www.sciencedirect.com/science/article/pii/0020768380900529` doi: https://doi.org/10.1016/0020-7683(80)90052-9

Goodman, J., & Weare, J. (2010, January). Ensemble samplers with affine invariance. *Communications in Applied Mathematics and Computational Science*,

5(1), 65-80. doi: 10.2140/camcos.2010.5.65

Goossens, S., Matsumoto, K., Liu, Q., Kikuchi, F., Sato, K., Hanada, H., ... Chen, M. (2011, April). Lunar gravity field determination using SELENE same-beam differential VLBI tracking data. *Journal of Geodesy*, *85*(4), 205-228. doi: 10.1007/s00190-010-0430-2

Goossens, S., Renaud, J. P., Henning, W. G., Mazarico, E., Bertone, S., & Genova, A. (2022, February). Evaluation of Recent Measurements of Mercury's Moments of Inertia and Tides Using a Comprehensive Markov Chain Monte Carlo Method. *The Planetary Science Journal*, *3*(2), 37. doi: 10.3847/PSJ/ac4bb8

Harada, Y., Goossens, S., Matsumoto, K., Yan, J., Ping, J., Noda, H., & Haruyama, J. (2014, August). Strong tidal heating in an ultralow-viscosity zone at the core-mantle boundary of the Moon. *Nature Geoscience*, *7*(8), 569-572. doi: 10.1038/ngeo2211

Harada, Y., Goossens, S., Matsumoto, K., Yan, J., Ping, J., Noda, H., & Haruyama, J. (2016, September). The deep lunar interior with a low-viscosity zone: Revised constraints from recent geodetic parameters on the tidal response of the Moon. *Icarus*, *276*, 96-101. doi: 10.1016/j.icarus.2016.04.021

Hirth, G., & Kohlstedt, D. L. (1996, October). Water in the oceanic upper mantle: implications for rheology, melt extraction and the evolution of the lithosphere. *Earth and Planetary Science Letters*, *144*(1-2), 93-108. doi: 10.1016/0012-821X(96)00154-9

Hu, X., Stark, A., Dirkx, D., Hussmann, H., Fienga, A., Fayolle-Chambe, M., ... Oberst, J. (2022, May). Sensitivity analysis of frequency-dependent viscoelastic effects on lunar orbiters. In *Egu general assembly conference abstracts* (p. EGU22-9722). doi: 10.5194/egusphere-egu22-9722

Jackson, I., Faul, U. H., & Skelton, R. (2014, March). Elastically accommodated grain-boundary sliding: New insights from experiment and modeling. *Physics of the Earth and Planetary Interiors*, *228*, 203-210. doi: 10.1016/j.pepi.2013.11.014

Jackson, I., Faul, U. H., Suetsugu, D., Bina, C., Inoue, T., & Jellinek, M. (2010, November). Grainsize-sensitive viscoelastic relaxation in olivine: Towards a robust laboratory-based model for seismological application. *Physics of the Earth and Planetary Interiors*, *183*(1-2), 151-163. doi: 10.1016/j.pepi.2010.09.005

Jacobs, M. H. G., van den Berg, A. P., Schmid-Fetzer, R., de Vries, J., van Westrenen, W., & Zhao, Y. (2022, July). Thermodynamic properties of geikielite ($MgTiO_3$) and ilmenite ($FeTiO_3$) derived from vibrational methods combined with Raman and infrared spectroscopic data. *Physics and Chemistry of Minerals*, *49*(7), 23. doi: 10.1007/s00269-022-01195-5

Jacobsen, S. D., Jiang, F., Mao, Z., Duffy, T. S., Smyth, J. R., Holl, C. M., & Frost, D. J. (2008, July). Effects of hydration on the elastic properties of olivine. *Geophysical Research Letters*, *35*(14), L14303. doi: 10.1029/2008GL034398

Jones, M. J., Evans, A. J., Johnson, B. C., Weller, M. B., Andrews-Hanna, J. C., Tikoo, S. M., & Keane, J. T. (2022, April). A South Pole–Aitken impact origin of the lunar compositional asymmetry. *Science Advances*, *8*(14), eabm8475. doi: 10.1126/sciadv.abm8475

Karato, S.-i. (2013, December). Geophysical constraints on the water content of the lunar mantle and its implications for the origin of the Moon. *Earth and Planetary Science Letters*, *384*, 144-153. doi: 10.1016/j.epsl.2013.10.001

Katz, R. F., Spiegelman, M., & Langmuir, C. H. (2003). A new parameterization of hydrous mantle melting. *Geochemistry, Geophysics, Geosystems*, *4*(9). Retrieved from `https://agupubs.onlinelibrary.wiley.com/doi/abs/10.1029/2002GC000433` doi: https://doi.org/10.1029/2002GC000433

Kawamura, T., Lognonné, P., Nishikawa, Y., & Tanaka, S. (2017, July). Evaluation of deep moonquake source parameters: Implication for fault characteristics and thermal state. *Journal of Geophysical Research (Planets)*, *122*(7), 1487-1504.

doi: 10.1002/2016JE005147

Kê, T.-S. (1947, April). Experimental Evidence of the Viscous Behavior of Grain Boundaries in Metals. *Physical Review*, *71*(8), 533-546. doi: 10.1103/PhysRev.71.533

Kervazo, M., Tobie, G., Choblet, G., Dumoulin, C., & Běhounková, M. (2021, June). Solid tides in Io's partially molten interior. Contribution of bulk dissipation. *Astronomy & Astrophysics*, *650*, A72. doi: 10.1051/0004-6361/202039433

Khan, A., Connolly, J. A. D., Pommier, A., & Noir, J. (2014, October). Geophysical evidence for melt in the deep lunar interior and implications for lunar evolution. *Journal of Geophysical Research (Planets)*, *119*(10), 2197-2221. doi: 10.1002/2014JE004661

Konopliv, A. S., Park, R. S., Yuan, D.-N., Asmar, S. W., Watkins, M. M., Williams, J. G., ... Zuber, M. T. (2013, July). The JPL lunar gravity field to spherical harmonic degree 660 from the GRAIL Primary Mission. *Journal of Geophysical Research (Planets)*, *118*(7), 1415-1434. doi: 10.1002/jgre.20097

Kraettli, G., Schmidt, M. W., & Liebske, C. (2022). Fractional crystallization of a basal lunar magma ocean: A dense melt-bearing garnetite layer above the core? *Icarus*, *371*, 114699. Retrieved from `https://www.sciencedirect.com/science/article/pii/S0019103521003547` doi: https://doi.org/10.1016/j.icarus.2021.114699

Kronrod, E., Matsumoto, K., Kuskov, O. L., Kronrod, V., Yamada, R., & Kamata, S. (2022, April). Towards geochemical alternatives to geophysical models of the internal structure of the lunar mantle and core. *Advances in Space Research*, *69*(7), 2798-2824. doi: 10.1016/j.asr.2022.01.012

Laneuville, M., Wieczorek, M. A., Breuer, D., & Tosi, N. (2013, July). Asymmetric thermal evolution of the Moon. *Journal of Geophysical Research (Planets)*, *118*(7), 1435-1452. doi: 10.1002/jgre.20103

Lee, L. C., & Morris, S. J. S. (2010, March). Anelasticity and grain boundary sliding. *Proceedings of the Royal Society of London Series A*, *466*(2121), 2651-2671. doi: 10.1098/rspa.2009.0624

Lee, L. C., Morris, S. J. S., & Wilkening, J. (2011, June). Stress concentrations, diffusionally accommodated grain boundary sliding and the viscoelasticity of polycrystals. *Proceedings of the Royal Society of London Series A*, *467*(2130), 1624-1644. doi: 10.1098/rspa.2010.0447

Lemoine, F. G., Goossens, S., Sabaka, T. J., Nicholas, J. B., Mazarico, E., Rowlands, D. D., ... Zuber, M. T. (2013, August). High−degree gravity models from GRAIL primary mission data. *Journal of Geophysical Research (Planets)*, *118*(8), 1676-1698. doi: 10.1002/jgre.20118

Li, H., Zhang, N., Liang, Y., Wu, B., Dygert, N. J., Huang, J., & Parmentier, E. M. (2019). Lunar cumulate mantle overturn: A model constrained by ilmenite rheology. *Journal of Geophysical Research: Planets*, *124*(5), 1357-1378. Retrieved from `https://agupubs.onlinelibrary.wiley.com/doi/abs/10.1029/2018JE005905` doi: https://doi.org/10.1029/2018JE005905

Mao, Z., Fan, D., Lin, J.-F., Yang, J., Tkachev, S. N., Zhuravlev, K., & Prakapenka, V. B. (2015, September). Elasticity of single-crystal olivine at high pressures and temperatures. *Earth and Planetary Science Letters*, *426*, 204-215. doi: 10.1016/j.epsl.2015.06.045

Matsumoto, K., Yamada, R., Kikuchi, F., Kamata, S., Ishihara, Y., Iwata, T., ... Sasaki, S. (2015, September). Internal structure of the Moon inferred from Apollo seismic data and selenodetic data from GRAIL and LLR. *Geophysical Research Letters*, *42*(18), 7351-7358. doi: 10.1002/2015GL065335

Matsuyama, I., Nimmo, F., Keane, J. T., Chan, N. H., Taylor, G. J., Wieczorek, M. A., ... Williams, J. G. (2016, August). GRAIL, LLR, and LOLA constraints on the interior structure of the Moon. *Geophysical Research Letters*, *43*(16), 8365-8375. doi: 10.1002/2016GL069952

Mazarico, E., Barker, M. K., Neumann, G. A., Zuber, M. T., & Smith, D. E. (2014, April). Detection of the lunar body tide by the Lunar Orbiter Laser Altimeter. *Geophysical Research Letters*, *41*(7), 2282-2288. doi: 10.1002/2013GL059085

Morris, S. J. S., & Jackson, I. (2009, April). Diffusionally assisted grain-boundary sliding and viscoelasticity of polycrystals. *Journal of Mechanics and Physics of Solids*, *57*(4), 744-761. doi: 10.1016/j.jmps.2008.12.006

Mosegaard, K., & Tarantola, A. (1995, July). Monte Carlo sampling of solutions to inverse problems. *Journal of Geophysical Research*, *100*(B7), 12,431-12,447. doi: 10.1029/94JB03097

Nakamura, Y. (2005, January). Farside deep moonquakes and deep interior of the Moon. *Journal of Geophysical Research (Planets)*, *110*(E1), E01001. doi: 10.1029/2004JE002332

Nakamura, Y., Lammlein, D., Latham, G., Ewing, M., Dorman, J., Press, F., & Toksoz, N. (1973, July). New Seismic Data on the State of the Deep Lunar Interior. *Science*, *181*(4094), 49-51. doi: 10.1126/science.181.4094.49

Nakamura, Y., Latham, G., Lammlein, D., Ewing, M., Duennebier, F., & Dorman, J. (1974, January). Deep lunar interior inferred from recent seismic data. *Geophysical Research Letters*, *1*(3), 137-140. doi: 10.1029/GL001i003p00137

Nimmo, F., Faul, U. H., & Garnero, E. J. (2012, September). Dissipation at tidal and seismic frequencies in a melt-free Moon. *Journal of Geophysical Research (Planets)*, *117*(E9), E09005. doi: 10.1029/2012JE004160

Noyelles, B., Frouard, J., Makarov, V. V., & Efroimsky, M. (2014, October). Spin-orbit evolution of Mercury revisited. *Icarus*, *241*, 26-44. doi: 10.1016/j.icarus.2014.05.045

Nunn, C., Garcia, R. F., Nakamura, Y., Marusiak, A. G., Kawamura, T., Sun, D., ... Zhu, P. (2020, July). Lunar Seismology: A Data and Instrumentation Review. *Space Science Reviews*, *216*(5), 89. doi: 10.1007/s11214-020-00709-3

Panning, M., Kedar, S., Bowles, N., Calcutt, S., Cutler, J., Elliott, J., ... Yana, C. (2021, December). Farside Seismic Suite (FSS): First seismic data from the farside of the Moon delivered by a commercial lander. In *Agu fall meeting abstracts* (Vol. 2021, p. P54C-01). Retrieved from `https://www.hou.usra.edu/meetings/lpsc2022/pdf/1576.pdf`

Pavlov, D. A., Williams, J. G., & Suvorkin, V. V. (2016, November). Determining parameters of Moon's orbital and rotational motion from LLR observations using GRAIL and IERS-recommended models. *Celestial Mechanics and Dynamical Astronomy*, *126*(1-3), 61-88. doi: 10.1007/s10569-016-9712-1

Qin, C., Muirhead, A. C., & Zhong, S. (2012, July). Correlation of deep moonquakes and mare basalts: Implications for lunar mantle structure and evolution. *Icarus*, *220*(1), 100-105. doi: 10.1016/j.icarus.2012.04.023

Raevskiy, S. N., Gudkova, T. V., Kuskov, O. L., & Kronrod, V. A. (2015, January). On reconciling the models of the interior structure of the moon with gravity data. *Izvestiya, Physics of the Solid Earth*, *51*(1), 134-142. doi: 10.1134/S1069351315010127

Raj, R., & Ashby, M. F. (1971, January). On grain boundary sliding and diffusional creep. *Metallurgical Transactions*, *2*, 1113-1127. doi: 10.1007/BF02664244

Sabadini, R., & Vermeersen, B. (2004). *Global Dynamics of the Earth: Applications of Normal Mode Relaxation Theory to Solid-Earth Geophysics*. Dodrech, the Netherlands: Kluwer Academic Publishers.

Samuel, H., Ballmer, M. D., Padovan, S., Tosi, N., Rivoldini, A., & Plesa, A.-C. (2021, April). The Thermo Chemical Evolution of Mars With a Strongly Stratified Mantle. *Journal of Geophysical Research (Planets)*, *126*(4), e06613. doi: 10.1029/2020JE006613

Segatz, M., Spohn, T., Ross, M. N., & Schubert, G. (1988). Tidal Dissipation, Surface Heat Flow, and Figure of Viscoelastic Models of Io. *Icarus*, *75*(2), 187-206. doi: 10.1016/0019-1035(88)90001-2

Siegler, M. A., & Smrekar, S. E. (2014, January). Lunar heat flow: Regional prospective of the Apollo landing sites. *Journal of Geophysical Research (Planets)*, *119*(1), 47-63. doi: 10.1002/2013JE004453

Stähler, S. C., Khan, A., Banerdt, W. B., Lognonné, P., Giardini, D., Ceylan, S., ... Smrekar, S. E. (2021, July). Seismic detection of the martian core. *Science*, *373*(6553), 443-448. doi: 10.1126/science.abi7730

Stark, A., Xiao, H., Hu, X., Fienga, A., Hussmann, H., Oberst, J., ... Saliby, C. (2022, May). Measurement of tidal deformation through self-registration of laser profiles: Application to Earth's Moon. In *Egu general assembly conference abstracts* (p. EGU22-10626). doi: 10.5194/egusphere-egu22-10626

Steinbrügge, G., Dumberry, M., Rivoldini, A., Schubert, G., Cao, H., Schroeder, D. M., & Soderlund, K. M. (2021, February). Challenges on Mercury's Interior Structure Posed by the New Measurements of its Obliquity and Tides. *Geophys. Res. Lett.*, *48*(3), e89895. doi: 10.1029/2020GL089895

Sundberg, M., & Cooper, R. F. (2010). A composite viscoelastic model for incorporating grain boundary sliding and transient diffusion creep; correlating creep and attenuation responses for materials with a fine grain size. *Philosophical Magazine*, *90*(20), 2817-2840. Retrieved from `https://doi.org/10.1080/14786431003746656` doi: 10.1080/14786431003746656

Takeuchi, H., & Saito, M. (1972). Seismic Surface Waves. *Methods in Computational Physics: Advances in Research and Applications*, *11*, 217-295. doi: 10.1016/B978-0-12-460811-5.50010-6

Tan, Y., & Harada, Y. (2021, September). Tidal constraints on the low-viscosity zone of the Moon. *Icarus*, *365*, 114361. doi: 10.1016/j.icarus.2021.114361

Thor, R. N., Kallenbach, R., Christensen, U. R., Gläser, P., Stark, A., Steinbrügge, G., & Oberst, J. (2021, January). Determination of the lunar body tide from global laser altimetry data. *Journal of Geodesy*, *95*(1), 4. Retrieved from `https://www.hou.usra.edu/meetings/lpsc2022/pdf/1576.pdf` doi: 10.1007/s00190-020-01455-8

Tobie, G., Grasset, O., Lunine, J. I., Mocquet, A., & Sotin, S. (2005). Tidal dissipation within large icy satellites: Applications to Europa and Titan. *Icarus*, *175*(2), 496-502. doi: 10.1016/j.icarus.2004.12.007

van Kan Parker, M., Sanloup, C., Sator, N., Guillot, B., Tronche, E. J., Perrillat, J.-P., ... van Westrenen, W. (2012, March). Neutral buoyancy of titanium-rich melts in the deep lunar interior. *Nature Geoscience*, *5*(3), 186-189. doi: 10.1038/ngeo1402

Viswanathan, V., Fienga, A., Minazzoli, O., Bernus, L., Laskar, J., & Gastineau, M. (2018, May). The new lunar ephemeris INPOP17a and its application to fundamental physics. *Monthly Notices of the Royal Astronomical Society*, *476*(2), 1877-1888. doi: 10.1093/mnras/sty096

Viswanathan, V., Rambaux, N., Fienga, A., Laskar, J., & Gastineau, M. (2019, July). Observational Constraint on the Radius and Oblateness of the Lunar Core-Mantle Boundary. *Geophysical Research Letters*, *46*(13), 7295-7303. doi: 10.1029/2019GL082677

Weber, R. C., Lin, P.-Y., Garnero, E. J., Williams, Q., & Lognonné, P. (2011, January). Seismic Detection of the Lunar Core. *Science*, *331*(6015), 309. doi: 10.1126/science.1199375

Williams, J. G., & Boggs, D. H. (2009). Lunar Core and Mantle. What Does LLR See? In *Proceedings of the 16th international workshop on laser ranging held on 13-17 october 2008 in poznań, poland. edited by s. schilliak. published by: Space research centre, polish academy of sciences, warsaw* (p. 101-120). Retrieved from `http://cddis.gsfc.nasa.gov/lw16/docs/papers/proceedings\_vol2.pdf,http://cddis.gsfc.nasa.gov/lw16/docs/papers/sci\_1\_Williams\_p.pdf`

Williams, J. G., & Boggs, D. H. (2015, April). Tides on the Moon: Theory and de-

termination of dissipation. *Journal of Geophysical Research (Planets)*, *120*(4), 689-724. doi: 10.1002/2014JE004755

Williams, J. G., Boggs, D. H., & Ratcliff, J. T. (2012, March). Lunar Moment of Inertia, Love Number, and Core. In *43rd annual lunar and planetary science conference* (p. 2230).

Williams, J. G., Boggs, D. H., Yoder, C. F., Ratcliff, J. T., & Dickey, J. O. (2001, November). Lunar rotational dissipation in solid body and molten core. *Journal of Geophysical Research*, *106*(E11), 27933-27968. doi: 10.1029/2000JE001396

Williams, J. G., Konopliv, A. S., Boggs, D. H., Park, R. S., Yuan, D.-N., Lemoine, F. G., ... Zuber, M. T. (2014, July). Lunar interior properties from the GRAIL mission. *Journal of Geophysical Research (Planets)*, *119*(7), 1546-1578. doi: 10.1002/2013JE004559

Wu, P., & Peltier, W. R. (1982). Viscous gravitational relaxation. *Geophysical Journal International*, *70*(2), 435-485. doi: 10.1111/j.1365-246X.1982.tb04976.x

Wyatt, B. A. (1977, January). The melting and crystallisation behaviour of a natural clinopyroxene-ilmenite intergrowth. *Contributions to Mineralogy and Petrology*, *61*(1), 1-9. doi: 10.1007/BF00375941

Yan, J., Goossens, S., Matsumoto, K., Ping, J., Harada, Y., Iwata, T., ... Kawano, N. (2012, March). CEGM02: An improved lunar gravity model using Chang'E-1 orbital tracking data. *Planetary and Space Science*, *62*(1), 1-9. doi: 10.1016/j.pss.2011.11.010

Yan, J., Liu, S., Xiao, C., Ye, M., Cao, J., Harada, Y., ... Barriot, J.-P. (2020, April). A degree-100 lunar gravity model from the Chang'e 5T1 mission. *Astronomy & Astrophysics*, *636*, A45. doi: 10.1051/0004-6361/201936802

Zhang, N., Parmentier, E. M., & Liang, Y. (2013, September). A 3-D numerical study of the thermal evolution of the Moon after cumulate mantle overturn: The importance of rheology and core solidification. *Journal of Geophysical Research. Planets*, *118*(9), 1789-1804. doi: 10.1002/jgre.20121

Zhao, Y., de Vries, J., van den Berg, A. P., Jacobs, M. H. G., & van Westrenen, W. (2019, April). The participation of ilmenite-bearing cumulates in lunar mantle overturn. *Earth and Planetary Science Letters*, *511*, 1-11. doi: 10.1016/j.epsl.2019.01.022

Zharkov, V. N., & Gudkova, T. V. (2005, September). Construction of Martian Interior Model. *Solar System Research*, *39*(5), 343-373. doi: 10.1007/s11208-005-0049-7

Zhu, M.-H., Wünnemann, K., Potter, R. W. K., Kleine, T., & Morbidelli, A. (2019, August). Are the Moon's Nearside-Farside Asymmetries the Result of a Giant Impact? *Journal of Geophysical Research (Planets)*, *124*(8), 2117-2140. doi: 10.1029/2018JE005826